EUROPEAN ORGANISATION FOR NUCLEAR RESEARCH (CERN)

# Search for direct production of charginos, neutralinos and sleptons in final states with two leptons and missing transverse momentum in $pp$ collisions at $\sqrt{s}$ = 8 TeV with the ATLAS detector

The ATLAS Collaboration

## Abstract

Searches for the electroweak production of charginos, neutralinos and sleptons in final states characterized by the presence of two leptons (electrons and muons) and missing transverse momentum are performed using $20.3\,\mathrm{fb}^{-1}$ of proton-proton collision data at $\sqrt{s} = 8\,\mathrm{TeV}$ recorded with the ATLAS experiment at the Large Hadron Collider. No significant excess beyond Standard Model expectations is observed. Limits are set on the masses of the lightest chargino, next-to-lightest neutralino and sleptons for different lightest-neutralino mass hypotheses in simplified models. Results are also interpreted in various scenarios of the phenomenological Minimal Supersymmetric Standard Model.

## Contents

## 1   Introduction

Supersymmetry (SUSY) [1–9] is a spacetime symmetry that postulates for each Standard Model (SM) particle the existence of a partner particle whose spin differs by one-half unit. The introduction of these new particles provides a potential solution to the hierarchy problem [10–13]. If $R$-parity is conserved [14–18], as is assumed in this paper, SUSY particles are always produced in pairs and the lightest supersymmetric particle (LSP) emerges as a stable dark-matter candidate.

The charginos and neutralinos are mixtures of the bino, winos and higgsinos that are superpartners of the U(1), SU(2) gauge bosons and the Higgs bosons, respectively. Their mass eigenstates are referred to as $\tilde{\chi}_i^\pm$ ($i = 1, 2$) and $\tilde{\chi}_j^0$ ($j = 1, 2, 3, 4$) in the order of increasing masses. Even though the gluinos and squarks are produced strongly in $pp$ collisions, if the masses of the gluinos and squarks are large, the direct production of charginos, neutralinos and sleptons through electroweak interactions may dominate the production of SUSY particles at the Large Hadron Collider (LHC). Such a scenario is possible in the general framework of the phenomenological minimal supersymmetric SM (pMSSM) [19–21]. Naturalness suggests that third-generation sparticles and some of the charginos and neutralinos should have masses of a few hundred GeV [22, 23]. Light sleptons are expected in gauge-mediated [24–29] and anomaly-mediated [30, 31] SUSY breaking scenarios. Light sleptons could also play a role in the co-annihilation of neutralinos, allowing a dark matter relic density consistent with cosmological observations [32, 33].

This paper presents searches for electroweak production of charginos, neutralinos and sleptons using $20.3\,\mathrm{fb}^{-1}$ of proton-proton collision data with a centre-of-mass energy $\sqrt{s} = 8$ TeV collected at the LHC with the ATLAS detector. The searches target final states with two oppositely-charged leptons (electrons or muons) and missing transverse momentum. Similar searches [34, 35] have been performed using $\sqrt{s} = 7$ TeV data by the ATLAS and CMS experiments. The combined LEP limits on the selectron, smuon and chargino masses are $m_{\tilde{e}} > 99.9$ GeV, $m_{\tilde{\mu}} > 94.6$ GeV and $m_{\tilde{\chi}_1^\pm} > 103.5$ GeV [36–40]. The LEP selectron limit assumes gaugino mass unification and cannot be directly compared with the results presented here.

## 2 SUSY scenarios

Simplified models [41] are considered for optimization of the event selection and interpretation of the results. The LSP is the lightest neutralino $\tilde{\chi}_1^0$ in all SUSY scenarios considered, except in one scenario in which it is the gravitino $\tilde{G}$. All SUSY particles except for the LSP are assumed to decay promptly. In the electroweak production of $\tilde{\chi}_1^+ \tilde{\chi}_1^-$ and $\tilde{\chi}_1^\pm \tilde{\chi}_2^0$, $\tilde{\chi}_1^\pm$ and $\tilde{\chi}_2^0$ are assumed to be pure wino and mass degenerate, and only the $s$-channel production diagrams, $q\bar{q} \to (Z/\gamma)^* \to \tilde{\chi}_1^+ \tilde{\chi}_1^-$ and $q\bar{q}' \to W^{\pm*} \to \tilde{\chi}_1^\pm \tilde{\chi}_2^0$, are considered. The cross-section for $\tilde{\chi}_1^+ \tilde{\chi}_1^-$ production is 6 pb for a $\tilde{\chi}_1^\pm$ mass of 100 GeV and decreases to 10 fb at 450 GeV. The cross-section for $\tilde{\chi}_1^\pm \tilde{\chi}_2^0$ production is 11.5 pb for a degenerate $\tilde{\chi}_1^\pm / \tilde{\chi}_2^0$ mass of 100 GeV, and 40 fb for 400 GeV.

In the scenario in which the masses of the sleptons and sneutrinos lie between the $\tilde{\chi}_1^\pm$ and $\tilde{\chi}_1^0$ masses, the $\tilde{\chi}_1^\pm$ decays predominantly as $\tilde{\chi}_1^\pm \to (\tilde{\ell}^\pm \nu \text{ or } \ell^\pm \tilde{\nu}) \to \ell^\pm \nu \tilde{\chi}_1^0$. Figure 1(a) shows direct chargino-pair production, $pp \to \tilde{\chi}_1^+ \tilde{\chi}_1^-$, followed by the slepton-mediated decays. The final-state leptons can be either of the same flavour (SF = $e^+ e^-$ or $\mu^+ \mu^-$), or of different flavours (DF = $e^\pm \mu^\mp$). In this scenario, the masses of the three left-handed sleptons and three sneutrinos are assumed to be degenerate with $m_{\tilde{\ell}} = m_{\tilde{\nu}} = (m_{\tilde{\chi}_1^0} + m_{\tilde{\chi}_1^\pm})/2$. The $\tilde{\chi}_1^\pm$ is assumed to decay with equal branching ratios (1/6) into $\tilde{\ell}^\pm \nu$ and $\ell^\pm \tilde{\nu}$ for three lepton flavours, followed by $\tilde{\ell}^\pm \to \ell^\pm \tilde{\chi}_1^0$ or $\tilde{\nu} \to \nu \tilde{\chi}_1^0$ with a 100% branching ratio.
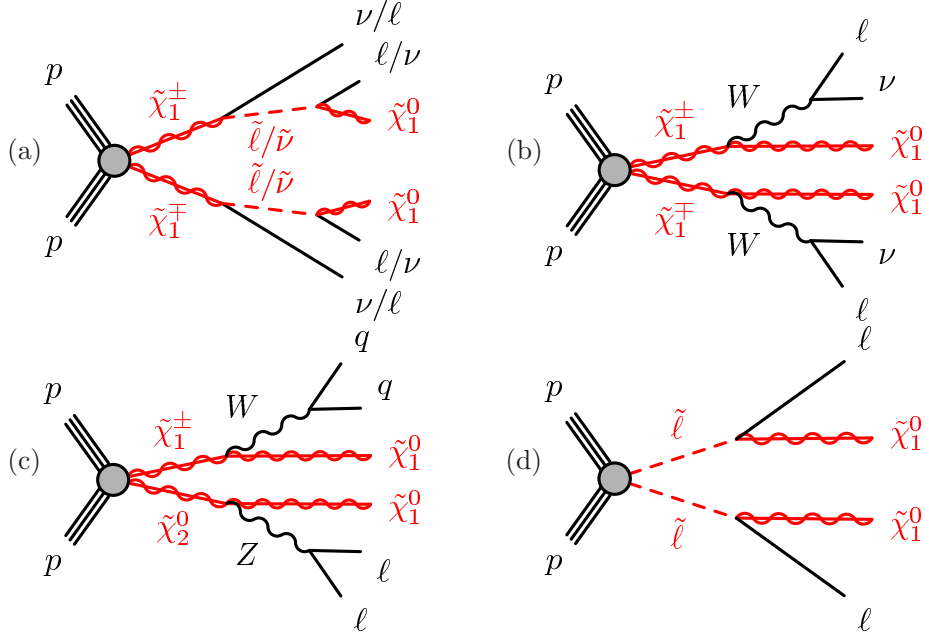
**Figure 1**. Electroweak SUSY production processes of the considered simplified models.

In the scenario in which the $\tilde{\chi}_1^\pm$ is the next-to-lightest supersymmetric particle (NLSP), the $\tilde{\chi}_1^\pm$ decays as $\tilde{\chi}_1^\pm \to W^\pm \tilde{\chi}_1^0$. In direct $\tilde{\chi}_1^+ \tilde{\chi}_1^-$ production, if both $W$ bosons decay leptonically as shown in figure 1(b), the final state contains two opposite-sign leptons, either SF or DF, and large missing transverse momentum.

Another scenario is considered in which $\tilde{\chi}_1^\pm$ and $\tilde{\chi}_2^0$ are mass degenerate and are co-NLSPs. The direct $\tilde{\chi}_1^\pm \tilde{\chi}_2^0$ production is followed by the decays $\tilde{\chi}_1^\pm \to W^\pm \tilde{\chi}_1^0$ and $\tilde{\chi}_2^0 \to Z \tilde{\chi}_1^0$ with a 100% branching fraction. If the $Z$ boson decays leptonically and the $W$ boson decays hadronically, as shown in figure 1(c), the final state contains two opposite-sign leptons, two hadronic jets, and missing transverse momentum. The leptons in this case are SF and their invariant mass is consistent with the $Z$ boson mass. The invariant mass of the two jets from the $W$ decay gives an additional constraint to characterize this signal.

A scenario in which the slepton is the NLSP is modelled according to ref. [42]. Figure 1(d) shows direct slepton-pair production $pp \to \tilde{\ell}^+ \tilde{\ell}^-$ followed by $\tilde{\ell}^\pm \to \ell^\pm \tilde{\chi}_1^0$ ($\ell = e$ or $\mu$), giving rise to a pair of SF leptons and missing transverse momentum due to the two neutralinos. The cross-section for direct slepton pair production in this scenario decreases from 127 fb to 0.5 fb per slepton flavour for left-handed sleptons, and from 49 fb to 0.2 fb for right-handed sleptons, as the slepton mass increases from 100 to 370 GeV.

Results are also interpreted in dedicated pMSSM [43] scenarios. In the models considered in this paper, the masses of the coloured sparticles, of the CP-odd Higgs boson, and of the left-handed sleptons are set to high values to allow only the direct production of charginos and neutralinos via $W/Z$, and their decay via right-handed sleptons, gauge bosons and the lightest Higgs boson. The lightest Higgs boson mass is set close to 125 GeV [44, 45] by tuning the mixing in the top squark sector. The mass hierarchy, com-

position and production cross-section of the charginos and neutralinos are governed by the ratio $\tan\beta$ of the expectation values of the two Higgs doublets, the gaugino mass parameters $M_1$ and $M_2$, and the higgsino mass parameter $\mu$. Two classes of pMSSM scenarios are studied on a $\mu$-$M_2$ grid, distinguished by the masses of the right-handed sleptons $\tilde{\ell}_R$. If $m_{\tilde{\ell}_R}$ lies halfway between $m_{\tilde{\chi}_1^0}$ and $m_{\tilde{\chi}_2^0}$, $\tilde{\chi}_2^0$ decays preferentially through $\tilde{\chi}_2^0 \to \tilde{\ell}_R \ell \to \tilde{\chi}_1^0 \ell\ell$. The parameter $\tan\beta$ is set to 6 yielding comparable branching ratios into each slepton generation. To probe the sensitivity to different $\tilde{\chi}_1^0$ compositions, three values of $M_1 = 100$, 140 and 250 GeV are considered. If, on the other hand, all sleptons are heavy, $\tilde{\chi}_1^\pm$ and $\tilde{\chi}_2^0$ decay via $W$, $Z$ and Higgs bosons. The remaining parameters are fixed to $\tan\beta = 10$ and $M_1 = 50$ GeV so that the relic dark-matter density is below the cosmological bound across the entire $\mu$-$M_2$ grid. The lightest Higgs boson has a mass close to 125 GeV and decays to both SUSY and SM particles where kinematically allowed.

In addition, the gauge-mediated SUSY breaking (GMSB) model proposed in ref. [46] is considered. In this simplified model, the LSP is the gravitino $\tilde{G}$, the NLSP is the chargino with $m_{\tilde{\chi}_1^\pm} = 110$ GeV, and in addition there are two other light neutralinos with masses $m_{\tilde{\chi}_1^0} = 113$ GeV and $m_{\tilde{\chi}_2^0} = 130$ GeV. All coloured sparticles are assumed to be very heavy. The $\tilde{\chi}_1^+\tilde{\chi}_1^-$ production cross-section is not large ($\sim 1.4$ pb), but the same final state is reached via production of $\tilde{\chi}_1^\pm\tilde{\chi}_1^0$ ($\sim 2.5$ pb), $\tilde{\chi}_1^\pm\tilde{\chi}_2^0$ ($\sim 1.0$ pb) and $\tilde{\chi}_1^0\tilde{\chi}_2^0$ ($\sim 0.5$ pb). The $\tilde{\chi}_1^0$ decays into $\tilde{\chi}_1^\pm W^{\mp*}$, and the $\tilde{\chi}_2^0$ decays either into $\tilde{\chi}_1^\pm W^{\mp*}$ or $\tilde{\chi}_1^0 Z^*$. Because of the small mass differences, decay products of the off-shell $W$ and $Z$ bosons are unlikely to be detected. As a result, all of the four production channels result in the same experimental signature, and their production cross-sections can be added together for the purpose of this search. Each $\tilde{\chi}_1^\pm$ then decays via $\tilde{\chi}_1^\pm \to W^\pm\tilde{G}$, and leptonic decays of the two $W$ bosons produce the same final-state as in the other scenarios.

## 3 The ATLAS detector

The ATLAS detector [47] is a multi-purpose particle physics detector with a forward-backward symmetric cylindrical geometry and nearly $4\pi$ coverage in solid angle[1]. It contains four superconducting magnet systems, which include a thin solenoid surrounding the inner tracking detector (ID), and barrel and end-cap toroids as part of a muon spectrometer (MS). The ID covers the pseudorapidity region $|\eta| < 2.5$ and consists of a silicon pixel detector, a silicon microstrip detector, and a transition radiation tracker. In the pseudorapidity region $|\eta| < 3.2$, high-granularity liquid-argon (LAr) electromagnetic (EM) sampling calorimeters are used. An iron-scintillator tile calorimeter provides coverage for hadron detection over $|\eta| < 1.7$. The end-cap and forward regions, spanning $1.5 < |\eta| < 4.9$, are instrumented with LAr calorimeters for both EM and hadronic measurements. The

---

[1] ATLAS uses a right-handed coordinate system with its origin at the nominal interaction point (IP) in the centre of the detector, and the $z$-axis along the beam line. The $x$-axis points from the IP to the centre of the LHC ring, and the $y$-axis points upwards. Cylindrical coordinates $(r, \phi)$ are used in the transverse plane, $\phi$ being the azimuthal angle around the $z$-axis. Observables labelled 'transverse' are projected into the $x$–$y$ plane. The pseudorapidity is defined in terms of the polar angle $\theta$ by $\eta = -\ln\tan(\theta/2)$.

MS surrounds the calorimeters and consists of a system of precision tracking chambers ($|\eta| < 2.7$), and detectors for triggering ($|\eta| < 2.4$).

## 4 Monte Carlo simulation

Monte Carlo (MC) simulated event samples are used to develop and validate the analysis procedure and to evaluate the subdominant SM backgrounds as well as the expected signal yields. The dominant SM background processes include $t\bar{t}$, single-top, and diboson ($WW$, $WZ$ and $ZZ$) production. The predictions for the most relevant SM processes are normalized to data in dedicated control regions, as detailed in section 7. MC samples are produced using a GEANT4 [48] based detector simulation [49] or a fast simulation using a parameterization of the performance of the ATLAS electromagnetic and hadronic calorimeters [50, 51] and GEANT4 elsewhere. The effect of multiple proton-proton collisions from the same or different bunch crossings is incorporated into the simulation by overlaying minimum bias events generated using PYTHIA [52] onto hard scatter events. Simulated events are weighted to match the distribution of the number of interactions per bunch crossing observed in data.

Production of top-quark pairs is simulated at next-to-leading order (NLO) with MC@NLO v4.06 [53–55], assuming a top-quark mass of 172.5 GeV. Additional samples generated with POWHEG-BOX v1.0 [56] and AcerMC v3.8 [57] are used for the evaluation of systematic uncertainties. The $t\bar{t}$ cross-section is normalized to the next-to-next-to-leading order (NNLO) calculation including resummation of next-to-next-to-leading logarithmic (NNLL) soft gluon terms obtained with Top++ v2.0 [58]. Single top production is modelled with MC@NLO v4.06 for $Wt$ and $s$-channel production, and with AcerMC v3.8 for $t$-channel production. Production of $t\bar{t}$ associated with a vector boson is simulated with the leading-order (LO) generator MADGRAPH 5 v1.3.33 [59] and normalized to the NLO cross-section [60–62].

Diboson ($WW$, $WZ$ and $ZZ$) production is simulated with POWHEG-BOX v1.0, with additional gluon-gluon contributions simulated with gg2WW v3.1.2 [63] and gg2ZZ v3.1.2 [64]. Additional diboson samples are generated at the particle level with aMC@NLO v2.0 [65] to assess systematic uncertainties. The diboson cross-sections are normalized to NLO QCD predictions obtained with MCFM v6.2 [66, 67]. Triple-boson ($WWW$, $ZWW$ and $ZZZ$) production is simulated with MADGRAPH 5 v1.3.33 [68], and vector-boson scattering ($WWjj$ and $WZjj$) is simulated with SHERPA v1.4.1 [69].

Samples of $W \to \ell\nu$ and $Z/\gamma^* \to \ell\ell$ produced with accompanying jets (including light and heavy flavours) are obtained with a combination of SHERPA v1.4.1 and ALPGEN v2.14 [70]. The inclusive $W$ and $Z/\gamma^*$ production cross-sections are normalized to the NNLO cross-sections obtained using DYNNLO v1.1 [71]. QCD production of $b\bar{b}$ and $c\bar{c}$ is simulated with PYTHIA v8.165.

Finally, production of the SM Higgs boson with $m_H = 125$ GeV is considered. The gluon fusion and vector-boson fusion production modes are simulated with POWHEG-BOX v1.0, and the associated production ($WH$ and $ZH$) with PYTHIA v8.165.

Fragmentation and hadronization for the MC@NLO and ALPGEN samples are performed either with HERWIG v6.520 [72] using JIMMY v4.31 [73] for the underlying event, or with

PYTHIA v6.426. PYTHIA v6.426 is also used for MADGRAPH samples, whereas PYTHIA v8.165 is used for the POWHEG-BOX samples. For the underlying event, ATLAS tune AUET2B [74] is used. The CT10 NLO [75] and CTEQ6L1 [76] parton-distribution function (PDF) sets are used with the NLO and LO event generators, respectively.

Simulated signal samples are generated with HERWIG++ v2.5.2 [77] and the CTEQ6L1 PDF set. Signal cross-sections are calculated to NLO using PROSPINO2.1 [78]. They are in agreement with the NLO calculations matched to resummation at the next-to-leading logarithmic accuracy (NLO+NLL) within $\sim 2\%$ [79–81].

## 5 Event reconstruction

Events are selected in which at least five tracks, each with transverse momentum $p_{\mathrm{T}} > 400$ MeV, are associated to the primary vertex. If there are multiple primary vertices in an event, the one with the largest $\sum p_{\mathrm{T}}^2$ of the associated tracks is chosen. In each event, 'candidate' electrons, muons, hadronically-decaying $\tau$ leptons, and jets are reconstructed. After resolving potential ambiguities among objects, the criteria to define 'signal' electrons, muons and jets are refined. Hadronically-decaying $\tau$ leptons are not considered as signal leptons for this analysis, and events containing them are removed (see section 6) so that the data sample is distinct from that used in the ATLAS search for electroweak SUSY production in the three-lepton final states [82].

Electron candidates are reconstructed by matching clusters in the EM calorimeter with tracks in the ID. The magnitude of the momentum of the electron is determined by the calorimeter cluster energy. They are required to have $p_{\mathrm{T}} > 10$ GeV, $|\eta| < 2.47$, and satisfy shower-shape and track-selection criteria analogous to the 'medium' criteria in ref. [83].

Muon candidates are reconstructed by matching an MS track to an ID track [84]. They are then required to have $p_{\mathrm{T}} > 10$ GeV and $|\eta| < 2.4$.

Jet candidates are reconstructed from calorimeter energy clusters using the anti-$k_t$ jet clustering algorithm [85, 86] with a radius parameter of 0.4. The jet candidates are corrected for the effects of calorimeter response and inhomogeneities using energy- and $\eta$-dependent calibration factors based on simulation and validated with extensive test-beam and collision-data studies [87]. Energy deposition due to pile-up interactions is statistically subtracted based on the area of the jet [88]. Only jet candidates with $p_{\mathrm{T}} > 20$ GeV and $|\eta| < 4.5$ are subsequently retained. Events containing jets that are likely to have arisen from detector noise or cosmic rays are removed [87].

A $b$-jet identification algorithm [89] is used to identify jets containing a $b$-hadron decay inside a candidate jet within $|\eta| < 2.4$, exploiting the long lifetime of $b$- and $c$-hadrons. The mean nominal $b$-jet identification efficiency, determined from simulated $t\bar{t}$ events, is 80%. The misidentification (mis-tag) rates for $c$-jets and light-quark/gluon jets are approximately 30% and 4%, respectively. Small differences in the $b$-tagging performance observed between data and simulation are corrected for as functions of $p_{\mathrm{T}}$ of the jets.

Hadronically-decaying $\tau$ leptons are reconstructed by associating tracks with $p_{\mathrm{T}} > 1$ GeV passing minimum track quality requirements to calorimeter jets with $p_{\mathrm{T}} > 10$ GeV and $|\eta| < 2.5$. A multivariate discriminant is used to identify the jets as hadronic $\tau$

decays [90]. Their energy is determined by applying a simulation-based correction to the reconstructed energy in the calorimeter [91], and $p_T > 20$ GeV is required.

Object overlaps are defined in terms of $\Delta R = \sqrt{(\Delta\eta)^2 + (\Delta\phi)^2}$, where $\Delta\eta$ and $\Delta\phi$ are separations in $\eta$ and $\phi$. Potential ambiguities among objects are resolved by removing one or both of nearby object pairs in the following order: if two electron candidates are within $\Delta R = 0.05$ of each other, the electron with the smaller $p_T$ is removed; any jet within $\Delta R = 0.2$ of an electron candidate is removed; any $\tau$ candidate within $\Delta R = 0.2$ of an electron or a muon is removed; any electron or muon candidate within $\Delta R = 0.4$ of a jet is removed; if an electron candidate and a muon candidate are within $\Delta R = 0.01$ of each other, both are removed; if two muon candidates are within $\Delta R = 0.05$ of each other, both are removed; if the invariant mass of a SF opposite-sign lepton pair has an invariant mass less than 12 GeV, both are removed; and finally any jet within $\Delta R = 0.2$ of a $\tau$ candidate is removed.

Signal electrons are electron candidates satisfying the 'tight' criteria [83] placed on the ratio of calorimetric energy to track momentum, and the number of high-threshold hits in the transition radiation tracker. They are also required to be isolated. The $p_T$ scalar sum of tracks above 400 MeV within a cone of size $\Delta R = 0.3$ around each electron candidate (excluding the electron candidate itself) and associated to the primary vertex is required to be less than 16% of the electron $p_T$. The sum of transverse energies of the surrounding calorimeter clusters within $\Delta R = 0.3$ of each electron candidate, corrected for the deposition of energy from pile-up interactions, is required to be less than 18% of the electron $p_T$. The distance of closest approach of an electron candidate to the event primary vertex must be within five standard deviations in the transverse plane. The distance along the beam direction, $z_0$, must satisfy $|z_0 \sin\theta| < 0.4$ mm.

Signal muons are muon candidates satisfying the following criteria. The $p_T$ scalar sum of tracks above 400 MeV within a cone of size $\Delta R = 0.3$ around the muon candidate and associated to the primary vertex is required to be less than 16% of the muon $p_T$. The distance of closest approach of a muon candidate to the event primary vertex must be within three standard deviations in the transverse plane, and $|z_0 \sin\theta| < 1$ mm along the beam direction.

The efficiencies for electrons and muons to pass the reconstruction, identification and isolation criteria are measured in samples of $Z$ and $J/\psi$ leptonic decays, and corrections are applied to the simulated samples to reproduce the efficiencies in data.

Signal jets are jet candidates that are classified in three exclusive categories. Central $b$-jets satisfy $|\eta| < 2.4$ and the $b$-jet identification criteria. Central light-flavour jets also satisfy $|\eta| < 2.4$ but do not satisfy the $b$-jet identification criteria. If a central light-flavour jet has $p_T < 50$ GeV and has tracks associated to it, at least one of the tracks must originate from the event primary vertex. This criterion removes jets that originate from pile-up interactions. Finally, forward jets are those with $2.4 < |\eta| < 4.5$ and $p_T > 30$ GeV.

The missing transverse momentum, $\mathbf{p}_T^{\mathrm{miss}}$, is defined [92] as the negative vector sum of the total transverse momenta of all $p_T > 10$ GeV electron, muon and photon candidates, $p_T > 20$ GeV jets, and all clusters of calorimeter energy with $|\eta| < 4.9$ not associated to such objects, referred to hereafter as the 'soft-term'. Clusters associated with electrons,

photons and jets make use of calibrations of the respective objects, whereas clusters not associated with these objects are calibrated using both calorimeter and tracker information.

The quantity $E_{\mathrm{T}}^{\mathrm{miss,rel}}$ is defined from the magnitude, $E_{\mathrm{T}}^{\mathrm{miss}}$, of $\mathbf{p}_{\mathrm{T}}^{\mathrm{miss}}$ as

$$E_{\mathrm{T}}^{\mathrm{miss,rel}} = \begin{cases} E_{\mathrm{T}}^{\mathrm{miss}} & \text{if } \Delta\phi_{\ell,j} \geq \pi/2 \\ E_{\mathrm{T}}^{\mathrm{miss}} \times \sin \Delta\phi_{\ell,j} & \text{if } \Delta\phi_{\ell,j} < \pi/2 \end{cases},$$

where $\Delta\phi_{\ell,j}$ is the azimuthal angle between the direction of $\mathbf{p}_{\mathrm{T}}^{\mathrm{miss}}$ and that of the nearest electron, muon, central $b$-jet or central light-flavour jet. Selections based on $E_{\mathrm{T}}^{\mathrm{miss,rel}}$ aim to suppress events where missing transverse momentum arises from significantly mis-measured jets or leptons.

## 6    Event selection

Events are recorded using a combination of two-lepton triggers, which require identification of two lepton (electron or muon) candidates with transverse momenta exceeding a set of thresholds. For all triggers used in this measurement, the $p_{\mathrm{T}}$ thresholds are 18–25 GeV for the higher-$p_{\mathrm{T}}$ lepton and 8–14 GeV for the other lepton. After event reconstruction, two signal leptons of opposite charge, with $p_{\mathrm{T}} > 35$ GeV and $> 20$ GeV, are required in the selected events. No lepton candidates other than the two signal leptons are allowed in the event. The two signal leptons are required to match those that triggered the event. The trigger efficiencies with respect to reconstructed leptons with $p_{\mathrm{T}}$ in excess of the nominal thresholds have been measured using data-driven techniques. For events containing two reconstructed signal leptons with $p_{\mathrm{T}} > 35$ GeV and $> 20$ GeV, the average trigger efficiencies are approximately 97% in the $e^+e^-$ channel, 75% in the $e^\pm\mu^\mp$ channels, and 89% in the $\mu^+\mu^-$ channel.

The dilepton invariant mass $m_{\ell\ell}$ must be greater than 20 GeV in all flavour combinations. Events containing one or more $\tau$-jet candidates are rejected.

Seven signal regions (SRs) are defined in this analysis. The first three, collectively referred to as SR-$m_{\mathrm{T2}}$, are designed to provide sensitivity to sleptons either through direct production or in chargino decays. The next three, SR-$WW$, are designed to provide sensitivity to chargino-pair production followed by $W$ decays. The last signal region, SR-$Z$jets, is designed specifically for chargino and second lightest neutralino associated production followed by hadronic $W$ and leptonic $Z$ decays. The SF and DF event samples in each SR are considered separately. When a scenario that contributes to both SF and DF final states is considered, a simultaneous fit to the SF and DF samples is employed. All SRs of the same lepton flavour combination, except for SR-$Z$jets, overlap with each other and are not statistically independent. Table 1 summarizes the definitions of the SRs.

Five of the SRs exploit the 'stransverse' mass $m_{\mathrm{T2}}$ [93, 94], defined as

$$m_{\mathrm{T2}} = \min_{\mathbf{q}_{\mathrm{T}}} \left[ \max \left( m_{\mathrm{T}}(\mathbf{p}_{\mathrm{T}}^{\ell 1}, \mathbf{q}_{\mathrm{T}}), m_{\mathrm{T}}(\mathbf{p}_{\mathrm{T}}^{\ell 2}, \mathbf{p}_{\mathrm{T}}^{\mathrm{miss}} - \mathbf{q}_{\mathrm{T}}) \right) \right],$$

where $\mathbf{p}_{\mathrm{T}}^{\ell 1}$ and $\mathbf{p}_{\mathrm{T}}^{\ell 2}$ are the transverse momenta of the two leptons, and $\mathbf{q}_{\mathrm{T}}$ is a transverse vector that minimizes the larger of the two transverse masses $m_{\mathrm{T}}$. The latter is defined by

$$m_{\mathrm{T}}(\mathbf{p}_{\mathrm{T}}, \mathbf{q}_{\mathrm{T}}) = \sqrt{2(p_{\mathrm{T}} q_{\mathrm{T}} - \mathbf{p}_{\mathrm{T}} \cdot \mathbf{q}_{\mathrm{T}})}.$$

For SM $t\bar{t}$ and $WW$ events, in which two $W$ bosons decay leptonically and $\mathbf{p}_\mathrm{T}^\mathrm{miss}$ originates from the two neutrinos, the $m_\mathrm{T2}$ distribution has an upper end-point at the $W$ mass. For signal events, the undetected LSP contributes to $\mathbf{p}_\mathrm{T}^\mathrm{miss}$, and the $m_\mathrm{T2}$ end-point is correlated to the mass difference between the slepton or chargino and the lightest neutralino. For large values of this difference, the $m_\mathrm{T2}$ distribution for signal events extends significantly beyond the distributions of the $t\bar{t}$ and $WW$ events.

## 6.1 SR-$m_\mathrm{T2}$

SR-$m_\mathrm{T2}$ targets $\tilde{\chi}_1^+\tilde{\chi}_1^-$ production followed by slepton-mediated decays (figure 1(a)) and direct slepton pair production (figure 1(d)). Events are required to contain two opposite-sign signal leptons and no signal jets. Only SF channels are used in the search for direct slepton production, while the chargino-to-slepton decay search also uses DF channels. In the SF channels, the dilepton invariant mass $m_{\ell\ell}$ must be at least 10 GeV away from the $Z$ boson mass.

The dominant sources of background are diboson and top production ($t\bar{t}$ and $Wt$). Three signal regions, SR-$m_\mathrm{T2}^{90}$, SR-$m_\mathrm{T2}^{120}$ and SR-$m_\mathrm{T2}^{150}$, are defined by requiring $m_\mathrm{T2} > 90$ GeV, 120 GeV and 150 GeV, respectively. Low values of $m_\mathrm{T2}$ threshold provide better sensitivity to cases in which the $\tilde{\ell}$ or $\tilde{\chi}_1^\pm$ mass is close to the $\tilde{\chi}_1^0$ mass, and high values target large $\tilde{\ell}$–$\tilde{\chi}_1^0$ or $\tilde{\chi}_1^\pm$–$\tilde{\chi}_1^0$ mass differences.

## 6.2 SR-$WW$

Direct $\tilde{\chi}_1^+\tilde{\chi}_1^-$ production followed by $W$-mediated decays (figure 1(b)) is similar to the slepton-mediated scenario, but with smaller visible cross-sections due to the $W \to \ell\nu$ branching fraction. Three signal regions, SR-$WW$a, SR-$WW$b and SR-$WW$c, are designed to provide sensitivities to this scenario for increasing values of $\tilde{\chi}_1^\pm$–$\tilde{\chi}_1^0$ mass difference. Events are required to contain two opposite-sign signal leptons and no signal jets. Both SF and DF channels are used in these signal regions. In the SF channels, the dilepton invariant mass $m_{\ell\ell}$ must be at least 10 GeV away from the $Z$ boson mass.

For large $\tilde{\chi}_1^\pm$–$\tilde{\chi}_1^0$ mass splitting, the $m_\mathrm{T2}$ variable provides good discrimination between the signal and SM background. Two signal regions, SR-$WW$b and SR-$WW$c, are defined by $m_\mathrm{T2} > 90$ GeV and 100 GeV, respectively. The $m_\mathrm{T2}$ thresholds are lower than in SR-$m_\mathrm{T2}$ because the smaller visible cross-sections limit the sensitivity to large $\tilde{\chi}_1^\pm$ masses. For SR-$WW$b, an additional requirement of $m_{\ell\ell} < 170$ GeV is applied to further suppress the SM background.

For cases in which the $\tilde{\chi}_1^\pm$–$\tilde{\chi}_1^0$ mass splitting is close to the $W$ boson mass, the $m_\mathrm{T2}$ variable is not effective in distinguishing signal from the SM $WW$ production. The signal region SR-$WW$a is defined by $E_\mathrm{T}^\mathrm{miss,rel} > 80$ GeV, $p_{\mathrm{T},\ell\ell} > 80$ GeV and $m_{\ell\ell} < 120$ GeV, where $p_{\mathrm{T},\ell\ell}$ is the transverse momentum of the lepton pair. These selection criteria favour events in which the di-lepton opening angle is small, which enhances the difference in the $E_\mathrm{T}^\mathrm{miss,rel}$ distribution between the signal and the background due to the two LSPs in the signal.

**Table 1**. Signal region definitions. The criteria on $|m_{\ell\ell} - m_Z|$ are applied only to SF events. The two leading central light jets in SR-$Z$jets must have $p_T > 45$ GeV.

| SR | $m_{\text{T2}}^{90}$ | $m_{\text{T2}}^{120}$ | $m_{\text{T2}}^{150}$ | $WW$a | $WW$b | $WW$c | $Z$jets |
|---|---|---|---|---|---|---|---|
| lepton flavour | DF,SF | DF,SF | DF,SF | DF,SF | DF,SF | DF,SF | SF |
| central light jets | 0 | 0 | 0 | 0 | 0 | 0 | $\geq 2$ |
| central $b$-jets | 0 | 0 | 0 | 0 | 0 | 0 | 0 |
| forward jets | 0 | 0 | 0 | 0 | 0 | 0 | 0 |
| $|m_{\ell\ell} - m_Z|$ [GeV] | $> 10$ | $> 10$ | $> 10$ | $> 10$ | $> 10$ | $> 10$ | $< 10$ |
| $m_{\ell\ell}$ [GeV] | — | — | — | $< 120$ | $< 170$ | — | — |
| $E_{\text{T}}^{\text{miss,rel}}$ [GeV] | — | — | — | $> 80$ | — | — | $> 80$ |
| $p_{\text{T},\ell\ell}$ [GeV] | — | — | — | $> 80$ | — | — | $> 80$ |
| $m_{\text{T2}}$ [GeV] | $> 90$ | $> 120$ | $> 150$ | — | $> 90$ | $> 100$ | — |
| $\Delta R_{\ell\ell}$ | — | — | — | — | — | — | [0.3,1.5] |
| $m_{jj}$ [GeV] | — | — | — | — | — | — | [50,100] |

### 6.3 SR-$Z$jets

The last signal region, SR-$Z$jets, differs from the previous six in that it requires the presence of at least two central light jets. This signal region is designed to target the $pp \to \tilde{\chi}_1^{\pm}\tilde{\chi}_2^0 \to W^{\pm}\tilde{\chi}_1^0 Z\tilde{\chi}_1^0$ process in which the $W$ boson decays hadronically and the $Z$ boson decays leptonically (figure 1(c)).

The two highest-$p_T$ central light jets must have $p_T > 45$ GeV, and have an invariant mass in the range $50 < m_{jj} < 100$ GeV. There must be no central $b$-jet and no forward jet in the event. The two opposite-sign leptons must be SF, and their invariant mass must be within 10 GeV of the $Z$ boson mass.

To suppress large background from the SM $Z$ + jets production, $E_{\text{T}}^{\text{miss,rel}} > 80$ GeV is required. Events are accepted only if the reconstructed $Z$ boson is recoiling against the rest of the event with a large transverse momentum $p_{\text{T},\ell\ell} > 80$ GeV, and the separation $\Delta R_{\ell\ell}$ between the two leptons must satisfy $0.3 < \Delta R_{\ell\ell} < 1.5$.

## 7 Background estimation

For SR-$m_{\text{T2}}$ and SR-$WW$, the SM background is dominated by $WW$ diboson and top-quark ($t\bar{t}$ and $Wt$) production. Contributions from $ZV$ production, where $V = W$ or $Z$, are also significant in the SF channels. The MC predictions for these background sources are normalized in dedicated control regions (CR) for each background, as described in section 7.1. For SR-$Z$jets, the dominant sources of background are $ZV$ production and $Z/\gamma^* +$ jets. The former is estimated from simulation, validated using $ZV$-enriched control samples, and the latter is estimated by a data-driven technique, as described in section 7.2. The top-quark background in SR-$Z$jets is estimated using a dedicated CR. Background due to hadronic jets mistakenly reconstructed as signal leptons or real leptons originating from heavy-flavour decays or photon conversions, referred to as 'non-prompt

**Table 2**. Control region definitions. The top CR for SR-$Z$jets requires at least two jets with $p_\mathrm{T} > 20$ GeV in $|\eta| < 2.4$, at least one of which is $b$-tagged.

| SR | $m_{\mathrm{T2}}$ and $WW$b/c | | | $WW$a | | | $Z$jets |
|---|---|---|---|---|---|---|---|
| CR | $WW$ | Top | $ZV$ | $WW$ | Top | $ZV$ | Top |
| lepton flavour | DF | DF | SF | DF | DF | SF | SF |
| central light jets | 0 | 0 | 0 | 0 | 0 | 0 | $\geq 2$ |
| central $b$-jets | 0 | $\geq 1$ | 0 | 0 | $\geq 1$ | 0 | $\geq 1$ |
| forward jets | 0 | 0 | 0 | 0 | 0 | 0 | 0 |
| $|m_{\ell\ell} - m_Z|$ [GeV] | — | — | $< 10$ | — | — | $< 10$ | $> 10$ |
| $m_{\ell\ell}$ [GeV] | — | — | — | $< 120$ | $< 120$ | — | — |
| $E_\mathrm{T}^{\mathrm{miss,rel}}$ [GeV] | — | — | — | $[60, 80]$ | $> 80$ | $> 80$ | $> 80$ |
| $p_{\mathrm{T},\ell\ell}$ [GeV] | — | — | — | $> 40$ | $> 80$ | $> 80$ | $> 80$ |
| $m_{\mathrm{T2}}$ [GeV] | $[50, 90]$ | $> 70$ | $> 90$ | — | — | — | — |
| $\Delta R_{\ell\ell}$ | — | — | — | — | — | — | $[0.3, 1.5]$ |

leptons', is estimated using a data-driven method described in section 7.3. Contributions from remaining sources of SM background are small and are estimated from simulation. Table 2 summarizes the definitions of the control regions.

## 7.1  Background in SR-$m_{\mathrm{T2}}$ and SR-$WW$

The normalization factors for the background in SR-$m_{\mathrm{T2}}$ and SR-$WW$ due to the SM $WW$, top and $ZV$ production are constrained in dedicated CRs for each background. Each CR is dominated by the background of interest and is designed to be kinematically as close as possible to a corresponding signal region. The normalization factors are obtained from the likelihood fit described in section 7.4.

The $WW$ control region for SR-$m_{\mathrm{T2}}$ and SR-$WW$b/c is defined by requiring $50 < m_{\mathrm{T2}} < 90$ GeV and the events must contain no jets. Only the DF sample is used in this CR because the corresponding regions in the SF samples suffer from contamination from $Z/\gamma^* +$ jets background. Appropriate ratios of electron and muon efficiencies are used to obtain the SF background estimations from the corresponding DF CR. For SR-$WW$a, the CR is defined by lowering the $E_\mathrm{T}^{\mathrm{miss,rel}}$ and $p_{\mathrm{T},\ell}$ requirements so that $60 < E_\mathrm{T}^{\mathrm{miss,rel}} < 80$ GeV and $p_{\mathrm{T},\ell} > 40$ GeV. Figure 2(a) shows the $m_{\mathrm{T2}}$ distribution in this CR. The normalization factors are not applied to the MC predictions in all four plots of figure 2. Predicted signal contamination in this CR is less than 10% for the signal models $\tilde{\chi}_1^\pm \tilde{\chi}_1^\mp \to W^\pm W^\mp \tilde{\chi}_1^0 \tilde{\chi}_1^0$ with $m_{\tilde{\chi}_1^\pm} > 100$ GeV.

The top control region for SR-$m_{\mathrm{T2}}$ and SR-$WW$b/c is also defined using the DF sample, and by requiring at least one $b$-tagged jet and vetoing central light jets and forward jets. The events must also satisfy $m_{\mathrm{T2}} > 70$ GeV. Figure 2(b) shows the $E_\mathrm{T}^{\mathrm{miss,rel}}$ distribution in this CR. For SR-$WW$a, the CR is defined using the DF sample and requiring at least one $b$-tagged jet, with all the other SR criteria unchanged. The predicted contamination from SUSY signal is negligible for the models considered.
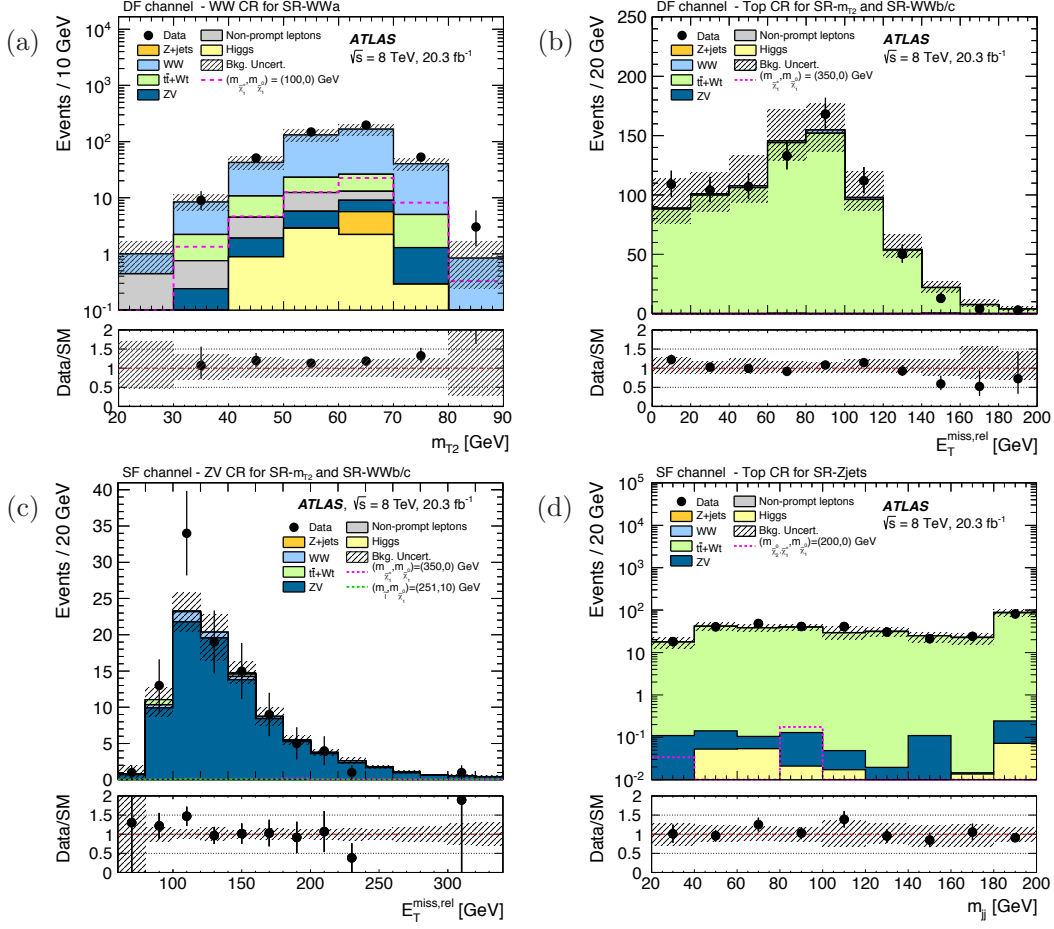
**Figure 2**. Distributions of (a) $m_{T2}$ in the $WW$ CR for SR-$WW$a, (b) $E_T^{miss,rel}$ in the top CR for SR-$WW$b/c and SR-$m_{T2}$, (c) $E_T^{miss,rel}$ in the $ZV$ CR for SR-$WW$b/c and SR-$m_{T2}$, and (d) $m_{jj}$ in the top CR for SR-$Z$jets. No data-driven normalization factor is applied to the distributions. The hashed regions represent the total uncertainties on the background estimates. The rightmost bin of each plot includes overflow. The lower panel of each plot shows the ratio between data and the SM background prediction.

The $ZV$ control region for SR-$m_{T2}$ and SR-$WW$b/c is defined identically to the SF SR-$m_{T2}^{90}$, but with the $Z$ veto reversed. Figure 2(c) shows the $E_T^{miss,rel}$ distribution in this CR. The contamination due to non-$ZV$ sources is dominated by $WW$ events (4.5%). For SR-$WW$a, the CR is defined by reversing the $Z$ veto in the SF sample. The predicted contamination from SUSY signal is less than 5% in these CRs.

### 7.2 Background in SR-$Z$jets

The top CR for SR-$Z$jets is defined by reversing the $Z$ veto and requiring at least one $b$-tagged jet. To increase the statistics of the sample, the $p_T$ threshold for the central jets is lowered to 20 GeV, and no cut on $m_{jj}$ is applied. Figure 2(d) shows the $m_{jj}$ distribution in this CR. The predicted contamination from SUSY signal is negligible.

The $ZV$ background in SR-$Z$jets consists of diboson production accompanied by two light-flavour jets, that is, $WZjj \to \ell\nu\ell'\ell'jj$, where the lepton from the $W$ decay was not reconstructed, and $ZZjj \to \ell\ell\nu\nu jj$. The contribution from $ZV \to \ell\ell q\bar{q}$ is strongly suppressed by the $E_{\mathrm{T}}^{\mathrm{miss,rel}}$ requirement. This background is estimated from simulation, and validated in control samples of $WZjj \to \ell\nu\ell'\ell'jj$ and $ZZjj \to \ell\ell\ell'\ell'jj$ where all leptons are reconstructed. The $WZjj$ enriched control sample consists of events with three leptons, at least two of which make up a SF opposite-sign pair with an invariant mass within 10 GeV of the $Z$ boson mass. In addition, events must have $E_{\mathrm{T}}^{\mathrm{miss}} > 30$ GeV, $m_{\mathrm{T}} > 40$ GeV computed from the $\mathbf{p}_{\mathrm{T}}^{\mathrm{miss}}$ and the lepton that was not assigned to the $Z$ boson, at least two central light jets, and no central $b$-jet. The predicted contamination from SUSY signal is less than 10% in this region. The $ZZjj$ enriched control sample consists of events with two pairs of same-flavour opposite-sign leptons, each with an invariant mass within 10 GeV of the $Z$ boson mass, $E_{\mathrm{T}}^{\mathrm{miss}} < 50$ GeV, at least two central light jets, and no signal $b$-jet. The data in these control samples are compared with the simulation to assess the systematic uncertainties of the $ZV$ background estimation, as reported in section 8.

In SR-$Z$jets, $Z/\gamma^* + $ jets events are an important source of background, where significant $E_{\mathrm{T}}^{\mathrm{miss}}$ arises primarily from mis-measurement of jet transverse momentum. A data-driven approach called the 'jet smearing' method is used to estimate this background. In this method, a sample enriched in $Z/\gamma^* + $ jets events with well-measured jets is selected from data as seed events. The seed events are selected by applying the SR-$Z$jets event selection, but reversing the $E_{\mathrm{T}}^{\mathrm{miss,rel}}$ cut. To ensure that the events only contain well measured jets, the ratio $E_{\mathrm{T}}^{\mathrm{miss}}/\sqrt{E_{\mathrm{T}}^{\mathrm{sum}}}$, where $E_{\mathrm{T}}^{\mathrm{sum}}$ is the scalar sum of the transverse energies of the jets and the soft-term, is required to be less than $1.5\,(\mathrm{GeV})^{1/2}$. Each seed event is smeared by multiplying each jet four-momentum by a random number drawn from the jet response function, which is initially estimated from simulation and adjusted after comparing the response to data in a photon $+$ jet sample. In addition, the contribution to $E_{\mathrm{T}}^{\mathrm{miss}}$ due to the soft-term is also modified by sampling randomly from the soft-term distribution measured in a $Z \to \ell\ell$ sample with no reconstructed jets. The smearing procedure is repeated 10,000 times for each seed event. The resulting pseudo-data $E_{\mathrm{T}}^{\mathrm{miss,rel}}$ distribution is then normalized to the data in the region of $E_{\mathrm{T}}^{\mathrm{miss,rel}} < 40$ GeV, and the migration into the signal region is evaluated.

To validate the jet-smearing method, a control sample is selected with the same selection criteria as SR-$Z$jets but reversing the $p_{\mathrm{T},\ell\ell}$ requirement, and removing the $\Delta R_{\ell\ell}$ and $m_{jj}$ criteria to increase the number of events. The seed events are selected from the control region events by requiring $E_{\mathrm{T}}^{\mathrm{miss,rel}} < 40$ GeV and $E_{\mathrm{T}}^{\mathrm{miss}}/\sqrt{E_{\mathrm{T}}^{\mathrm{sum}}} < 1.5\,(\mathrm{GeV})^{1/2}$. Results are validated in a region with $40 < E_{\mathrm{T}}^{\mathrm{miss,rel}} < 80$ GeV, which is dominated by $Z/\gamma^* + $ jets. The method predicts $750 \pm 100$ events, where both statistical and systematic uncertainties are included, in agreement with the 779 events observed in data.

## 7.3 Non-prompt lepton background estimation

The term 'non-prompt leptons' refers to hadronic jets mistakenly reconstructed as signal leptons or leptons originating from heavy-flavour decays or photon conversions. In this context, 'prompt leptons' are leptons produced directly in decays of sparticles or

weak bosons. The number of non-prompt lepton events is estimated using the matrix method [95], which takes advantage of the difference between the prompt efficiency $\epsilon_\mathrm{p}$ and non-prompt efficiency $\epsilon_\mathrm{n}$, defined as the fractions of prompt and non-prompt candidate leptons, respectively, that pass the signal-lepton requirements.

The prompt and non-prompt efficiencies are evaluated as functions of the $p_\mathrm{T}$ of the lepton candidate in simulated events using MC truth information. Differences between data and MC are corrected for with normalization factors measured in control samples. Since the efficiencies depend on the production process, average $\epsilon_\mathrm{p}$ and $\epsilon_\mathrm{n}$ values are calculated for each SR and CR using the fraction of each process predicted by the simulation as the weights. The data/MC normalization factors for $\epsilon_\mathrm{p}$ are derived from $Z \to \ell\ell$ events. The normalization factors for $\epsilon_\mathrm{n}$ depend on whether the non-prompt lepton originated from jets or from photon conversion. The normalization factors for misidentified jets or leptons from heavy-flavour decays are measured in a control region enriched in $b\bar{b}$ production. Events are selected with two candidate leptons, one $b$-tagged jet and $E_\mathrm{T}^\mathrm{miss,rel} < 40$ GeV. One of the two lepton candidates is required to be a muon and to lie within $\Delta R = 0.4$ of the $b$-tagged jet, while the other lepton candidate is used to measure the non-prompt efficiency. For measuring the normalization factor for photon conversions, a $Z \to \mu\mu\gamma$ control sample is defined by selecting events with two muons, $E_\mathrm{T}^\mathrm{miss,rel} < 50$ GeV, at least one candidate electron (which is the conversion candidate) with $m_\mathrm{T} < 40$ GeV, and requiring that the invariant mass of the $\mu^+\mu^-e^\pm$ system is within 10 GeV of the $Z$ boson mass.

Using $\epsilon_\mathrm{n}$ and $\epsilon_\mathrm{p}$, the observed numbers of events in each SR and CR with four possible combinations (signal-signal, signal-candidate, candidate-signal and candidate-candidate) of leptons are expressed as weighted sums of the numbers of events with four combinations of prompt and non-prompt leptons. Solving these equations allows determination of the non-prompt lepton background. The contribution of non-prompt-lepton background in the signal regions is less than 5% of the total background in all signal regions.

## 7.4   Fitting procedure

For each SR, a simultaneous likelihood fit to the corresponding CRs is performed to normalize the top, $WW$ and $ZV$ (in the case of SR-$Z$jets only top is fitted) background estimates. The inputs to the fit are the numbers of observed events in the CRs, the expected contributions of top, $WW$ and $ZV$ from simulation, and the expected contributions of other background sources determined as described in sections 7.1–7.3.

The event count in each CR is treated as a Poisson probability function, the mean of which is the sum of the expected contributions from all background sources. The free parameters in the fit are the normalization of the top, $WW$ and $ZV$ contributions. The systematic uncertainties on the expected background yields are included as nuisance parameters, constrained to be Gaussian with a width determined from the size of the uncertainty. Correlations between control and signal regions, and background processes are taken into account with common nuisance parameters. The free parameters and the nuisance parameters are determined by maximizing the product of the Poisson probability functions and the constraints on the nuisance parameters.

**Table 3**. Numbers of observed and predicted events in the CRs, data/MC normalization factors and composition of the CRs obtained from the fit. Systematic errors are described in section 8.

| SR | $m_{\mathrm{T2}}$ and $WW$b/c | | | $WW$a | | | $Z$jets |
|---|---|---|---|---|---|---|---|
| CR | $WW$ | Top | $ZV$ | $WW$ | Top | $ZV$ | Top |
| Observed events | 1061 | 804 | 94 | 472 | 209 | 175 | 395 |
| MC prediction | 947 | 789 | 91 | 385 | 215 | 162 | 399 |
| Normalization | 1.14 | 1.02 | 1.08 | 1.12 | 0.97 | 1.04 | 0.99 |
| Statistical error | 0.05 | 0.04 | 0.12 | 0.08 | 0.08 | 0.12 | 0.06 |
| Composition | | | | | | | |
| $WW$ | 84.6% | 1.4% | 5.0% | 86.8% | 1.7% | 10.5% | 1.3% |
| Top | 10.4% | 98.5% | <0.1% | 7.3% | 98.1% | 2.8% | 98.0% |
| $ZV$ | 2.0% | 0.1% | 94.9% | 1.9% | <0.1% | 82.9% | 0.3% |
| Non-prompt lepton | 1.9% | <0.1% | <0.1% | 2.7% | <0.1% | <0.1% | <0.1% |
| Other | 1.1% | <0.1% | 0.1% | 1.3% | <0.1% | 3.7% | 0.3% |

Table 3 summarizes the numbers of observed and predicted events in the CRs, data/MC normalization and CR composition obtained from the simultaneous fit. The normalization factors agree within errors between different SRs for each of the $WW$, Top and $ZV$ contributions. Results of the background estimates in the SRs can be found in Tables 5, 6 and 7.

# 8 Systematic uncertainties

Systematic uncertainties affect the estimates of the backgrounds and signal event yields in the control and signal regions. The relative sizes of the sources of systematic uncertainty on the total SM background in SR-$m_{\mathrm{T2}}$, SR-$WW$ and SR-$Z$jets are detailed in Table 4.

The 'CR statistics' and 'MC statistics' uncertainties arise from the number of data events in the CRs and simulated events in the SRs and CRs, respectively. The largest contributions are due to the simulated background samples in the signal regions.

The dominant experimental systematic uncertainties, labelled 'Jet' in Table 4, come from the propagation of the jet energy scale calibration [96] and resolution [97] uncertainties. They were derived from a combination of simulation, test-beam data and in situ measurements. Additional uncertainties due to differences between quark and gluon jets, and light and heavy flavour jets, as well as the effect of pile-up interactions are included. The 'Lepton' uncertainties include those from lepton reconstruction, identification and trigger efficiencies, as well as lepton energy and momentum measurements [83, 84]. Uncertainties due to $\tau$ reconstruction and energy calibration are negligible. Jet and lepton energy scale uncertainties are propagated to the $E_{\mathrm{T}}^{\mathrm{miss}}$ evaluation. An additional 'Soft-term' uncertainty is associated with the contribution to the $E_{\mathrm{T}}^{\mathrm{miss}}$ reconstruction of energy deposits not assigned to any reconstructed objects [92].

The '$b$-tagging' row refers to the uncertainties on the $b$-jet identification efficiency and charm and light-flavour jet rejection factors [98]. The 'Non-prompt lepton' uncertainties

**Table 4**. Systematic uncertainties (in %) on the total background estimated in different signal regions. Because of correlations between the systematic uncertainties and the fitted backgrounds, the total uncertainty can be different from the quadratic sum of the individual uncertainties.

| | $m_{\mathrm{T2}}^{90}$ | | $m_{\mathrm{T2}}^{120}$ | | $m_{\mathrm{T2}}^{150}$ | | $WW\mathrm{a}$ | | $WW\mathrm{b}$ | | $WW\mathrm{c}$ | | $Z$jets |
|---|---|---|---|---|---|---|---|---|---|---|---|---|---|
| | SF | DF | SF | DF | SF | DF | SF | DF | SF | DF | SF | DF | SF |
| CR statistics | 5 | 3 | 6 | 4 | 8 | 4 | 5 | 5 | 5 | 3 | 6 | 4 | 1 |
| MC statistics | 5 | 7 | 7 | 12 | 10 | 23 | 3 | 4 | 5 | 8 | 6 | 10 | 14 |
| Jet | 4 | 1 | 2 | 1 | 5 | 7 | 3 | 6 | 4 | 2 | 4 | 3 | 11 |
| Lepton | 1 | 2 | 1 | 1 | 4 | 1 | 1 | 3 | 2 | 3 | 1 | 8 | 4 |
| Soft-term | 3 | 4 | 1 | 1 | 2 | 8 | < 1 | 2 | 3 | 5 | 1 | 6 | 5 |
| b-tagging | 1 | 2 | <1 | <1 | <1 | <1 | 1 | 1 | 1 | 2 | <1 | 1 | 2 |
| Non-prompt lepton | <1 | 1 | <1 | <1 | 1 | <1 | 1 | 1 | 1 | 2 | <1 | 1 | <1 |
| Luminosity | <1 | <1 | <1 | <1 | <1 | <1 | <1 | <1 | <1 | <1 | <1 | <1 | 2 |
| Modelling | 11 | 13 | 21 | 31 | 18 | 40 | 6 | 6 | 8 | 10 | 15 | 19 | 42 |
| Total | 13 | 16 | 24 | 34 | 23 | 47 | 9 | 11 | 12 | 14 | 17 | 24 | 47 |

arise from the data-driven estimates of the non-prompt lepton background described in section 7.3. The dominant sources are $\eta$ dependencies of the non-prompt rates, differences between the light and heavy flavour jets, and the statistics of the control samples. The uncertainty on the integrated luminosity is $\pm 2.8\%$, and affects the normalization of the background estimated with simulation. It is derived following the methodology detailed in ref. [99].

The 'Modelling' field of Table 4 includes the uncertainties on the methods used for the background estimate, as well as the modelling uncertainties of the generators used to assist the estimate. For SR-$Z$jets an additional 20% uncertainty is assigned to the $ZV$ background estimate to account for the variations between data and simulation in the $ZV$ control regions with two or more jets, as described in section 7.2. Uncertainties on the $Z/\gamma^* +$ jets background estimate in SR-$Z$jets include the systematic uncertainties associated with the jet smearing method due to the fluctuations in the non-Gaussian tails of the response function and the systematic uncertainty associated with the cut value on $E_{\mathrm{T}}^{\mathrm{miss}}/\sqrt{E_{\mathrm{T}}^{\mathrm{sum}}}$ used to define the seed region. The effect of using each seed event multiple times is also taken into account. Generator modelling uncertainties are estimated by comparing the results from POWHEG and MC@NLO generators for top events, and POWHEG and aMC@NLO for $WW$ events, using HERWIG for parton showering in all cases. Parton showering uncertainties are estimated in top and $WW$ events by comparing POWHEG plus HERWIG with POWHEG plus PYTHIA. Both generator modelling and parton showering uncertainties are estimated in $ZV$ events by comparing POWHEG plus PYTHIA to SHERPA. Special $t\bar{t}$ samples are generated using AcerMC with PYTHIA to evaluate the uncertainties related to the amount of initial and final-state radiation [100]. Impact of the choice of renormalization and factorization scales is evaluated by varying them between 0.5 and 2 times the nominal values in POWHEG for top events and aMC@NLO for diboson events. The uncertainties due to the PDFs for the top and diboson events are evaluated using 90% C.L. CT10 PDF eigenvectors.

Effects of using different PDF sets have been found to be negligible. The dominant contribution among the 'Modelling' uncertainties comes from the difference between POWHEG and aMC@NLO for diboson production.

Signal cross-sections are calculated to NLO in the strong coupling constant. Their uncertainties are taken from an envelope of cross-section predictions using different PDF sets and factorization and renormalization scales, as described in ref. [101]. Systematic uncertainties associated with the signal selection efficiency include those due to lepton trigger, reconstruction and identification, jet reconstruction and $E_{\mathrm{T}}^{\mathrm{miss}}$ calculation. Uncertainties on the integrated luminosity affect the predicted signal yield. The total uncertainty on the predicted signal yield is typically 9–13% for SUSY scenarios to which this measurement is sensitive.

## 9   Results

Figures 3 and 4 show the comparison between data and the SM prediction for key kinematic variables in different signal regions. In each plot, the expected distributions from the $WW$, $t\bar{t}$ and $ZV$ processes are corrected with data-driven normalization factors obtained from the fit detailed in section 7. The hashed regions represent the sum in quadrature of systematic uncertainties and statistical uncertainties arising from the numbers of MC events. The effect of limited data events in the CR is included in the systematic uncertainty. All statistical uncertainties are added in quadrature whereas the systematic uncertainties are obtained after taking full account of all correlations between sources, background contributions and channels. The rightmost bin of each plot includes overflow. Illustrative SUSY benchmark models, normalized to the integrated luminosity, are superimposed. The lower panel of each plot shows the ratio between data and the SM background prediction.

Tables 5, 6 and 7 compare the observed yields in each signal region with those predicted for the SM background. The errors include both statistical and systematic uncertainties. Good agreement is observed across all channels.

For each SR, the significance of a possible excess over the SM background is quantified by the one-sided probability, $p_0$, of the background alone to fluctuate to the observed number of events or higher, using the asymptotic formula [102]. This is calculated using a fit similar to the one described in section 7.4, but including the observed number of events in the SR as an input. The accuracy of the limits obtained from the asymptotic formula was tested for all SRs by randomly generating a large number of pseudo data sets and repeating the fit. Upper limits at 95% CL on the number of non-SM events for each SR are derived using the $\mathrm{CL_s}$ prescription [103] and neglecting any possible contamination in the CRs. Normalizing these by the integrated luminosity of the data sample they can be interpreted as upper limits, $\sigma_{\mathrm{vis}}^{95}$, on the visible non-SM cross-section, defined as the product of acceptance, reconstruction efficiency and production cross-section of the non-SM contribution. All systematic uncertainties and their correlations are taken into account via nuisance parameters. The results are given in Tables 5, 6 and 7.
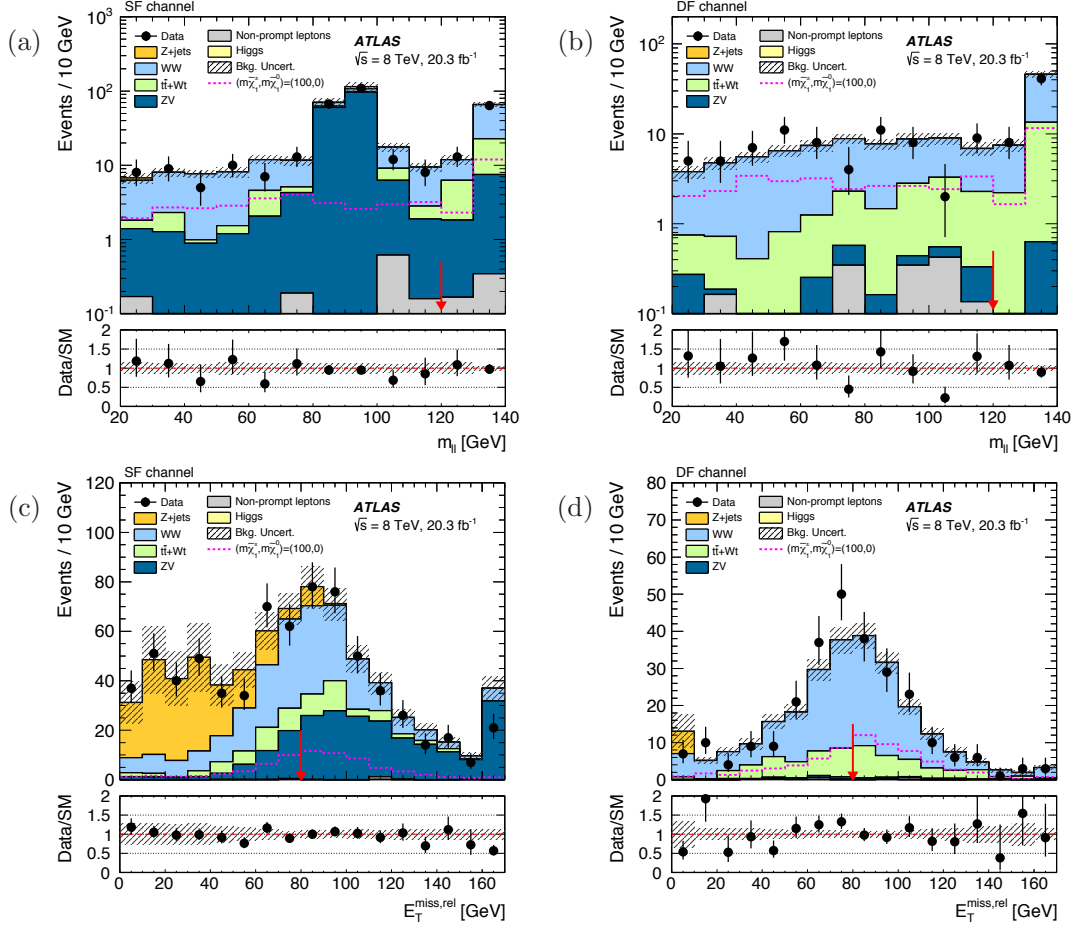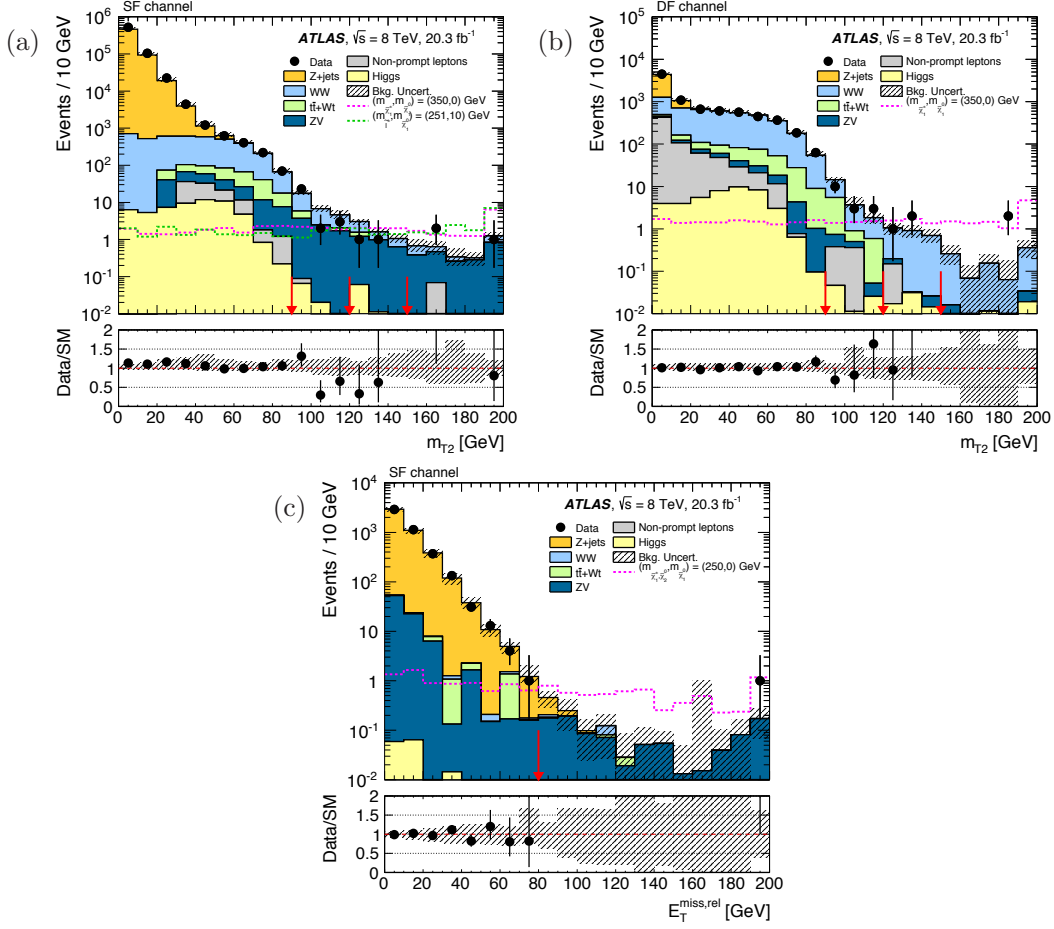
**Figure 3**. Distributions of $m_{\ell\ell}$ in the (a) SF and (b) DF samples that satisfy all the SR-$WW$a selection criteria except for the one on $m_{\ell\ell}$, and of $E_T^{miss,rel}$ in the (c) SF and (d) DF samples that satisfy all the SR-$WW$a selection criteria except for the ones on $m_{\ell\ell}$ and $E_T^{miss,rel}$. The lower panel of each plot shows the ratio between data and the SM background prediction. The hashed regions represent the sum in quadrature of systematic uncertainties and statistical uncertainties arising from the numbers of MC events. Predicted signal distributions in a simplified model with $m_{\tilde{\chi}_1^\pm} = 100$ GeV and $m_{\tilde{\chi}_1^0} = 0$ are superimposed. Red arrows indicate the SR-$WW$a selection criteria. In (a), the region $81.2 < m_{\ell\ell} < 101.2$ GeV is rejected by the $Z$ boson veto.

## 10   Interpretation

Exclusion limits at 95% confidence-level are set on the slepton, chargino and neutralino masses within the specific scenarios considered. The same CL$_s$ limit-setting procedure as in section 9 is used, except that the SUSY signal is allowed to populate both the signal region and the control regions as predicted by the simulation. Since the SRs are not mutually exclusive, the SR with the best expected exclusion limit is chosen for each model point.

The results are displayed in figures 5 through 9. In each exclusion plot, the solid (dashed) lines show observed (expected) exclusion contours, including all uncertainties

**Figure 4**. Distributions of $m_{T2}$ in the (a) SF and (b) DF samples that satisfy all the SR-$m_{T2}$ selection criteria except for the one on $m_{T2}$, and of (c) $E_T^{miss,rel}$ in the sample that satisfies all the SR-$Z$jets selection criteria except for the one on $E_T^{miss,rel}$. The lower panel of each plot shows the ratio between data and the SM background prediction. The hashed regions represent the sum in quadrature of systematic uncertainties and statistical uncertainties arising from the numbers of MC events. Predicted signal distributions in simplified models with $m_{\tilde{\chi}_1^\pm} = 350$ GeV, $m_{\tilde{\ell}} = m_{\tilde{\nu}} = 175$ GeV and $m_{\tilde{\chi}_1^0} = 0$ are superimposed in (a) and (b), $m_{\tilde{\ell}} = 251$ GeV and $m_{\tilde{\chi}_1^0} = 10$ GeV in (a), and $m_{\tilde{\chi}_1^\pm} = m_{\tilde{\chi}_2^0} = 250$ GeV and $m_{\tilde{\chi}_1^0} = 0$ in (c). Red arrows indicate the selection criteria for SR-$m_{T2}$ and SR-$Z$jets.

except for the theoretical signal cross-section uncertainty arising from the PDF and the renormalization and factorization scales. The solid band around the expected exclusion contour shows the $\pm 1\sigma$ result where all uncertainties, except those on the signal cross-sections, are considered. The dotted lines around the observed exclusion contour represent the results obtained when varying the nominal signal cross-section by $\pm 1\sigma$ theoretical uncertainty. All mass limits hereafter quoted correspond to the signal cross-sections reduced by $1\sigma$.

Figure 5 shows the 95% CL exclusion region obtained from SR-$m_{T2}$ on the simplified

**Table 5**. Observed and expected numbers of events in SR-$m_{\mathrm{T2}}$. Also shown are the one-sided $p_0$ values and the observed and expected 95% CL upper limits, $\sigma_{\mathrm{vis}}^{95}$, on the visible cross-section for non-SM events. The 'Others' background category includes non-prompt lepton, $Z/\gamma^* +$ jets and SM Higgs. The numbers of signal events are shown for the $\tilde{\chi}_1^+ \tilde{\chi}_1^- \rightarrow (\tilde{\ell}\nu$ or $\ell\tilde{\nu})\tilde{\chi}_1^0(\tilde{\ell}'\nu'$ or $\ell'\tilde{\nu}')\tilde{\chi}_1^0$ scenario and for the $\tilde{\ell}^+ \tilde{\ell}^- \rightarrow \ell^+ \tilde{\chi}_1^0 \ell^- \tilde{\chi}_1^0$ scenario with different $\tilde{\chi}_1^\pm$, $\tilde{\chi}_1^0$ and $\tilde{\ell}$ masses in GeV.

| | SR-$m_{\mathrm{T2}}^{90}$ | | SR-$m_{\mathrm{T2}}^{120}$ | | SR-$m_{\mathrm{T2}}^{150}$ | |
| --- | --- | --- | --- | --- | --- | --- |
| | SF | DF | SF | DF | SF | DF |
| Expected background | | | | | | |
| $WW$ | $22.1 \pm 4.3$ | $16.2 \pm 3.2$ | $3.5 \pm 1.3$ | $3.3 \pm 1.2$ | $1.0 \pm 0.5$ | $0.9 \pm 0.5$ |
| $ZV$ | $12.9 \pm 2.2$ | $0.8 \pm 0.2$ | $4.9 \pm 1.6$ | $0.2 \pm 0.1$ | $2.2 \pm 0.5$ | $< 0.1$ |
| Top | $3.0 \pm 1.8$ | $5.5 \pm 1.9$ | $0.3_{-0.3}^{+0.4}$ | $< 0.1$ | $< 0.1$ | $< 0.1$ |
| Others | $0.3 \pm 0.3$ | $0.8 \pm 0.6$ | $0.1_{-0.1}^{+0.4}$ | $0.1 \pm 0.1$ | $0.1_{-0.1}^{+0.4}$ | $0.0_{-0.0}^{+0.4}$ |
| Total | $38.2 \pm 5.1$ | $23.3 \pm 3.7$ | $8.9 \pm 2.1$ | $3.6 \pm 1.2$ | $3.2 \pm 0.7$ | $1.0 \pm 0.5$ |
| Observed events | 33 | 21 | 5 | 5 | 3 | 2 |
| Predicted signal | | | | | | |
| $(m_{\tilde{\chi}_1^\pm}, m_{\tilde{\chi}_1^0}) = (350, 0)$ | $24.2 \pm 2.5$ | $19.1 \pm 2.1$ | $18.1 \pm 1.8$ | $14.7 \pm 1.7$ | $12.0 \pm 1.3$ | $10.1 \pm 1.3$ |
| $(m_{\tilde{\ell}}, m_{\tilde{\chi}_1^0}) = (251, 10)$ | $24.0 \pm 2.7$ | — | $19.1 \pm 2.5$ | — | $14.3 \pm 1.7$ | — |
| $p_0$ | 0.50 | 0.50 | 0.50 | 0.27 | 0.50 | 0.21 |
| Observed $\sigma_{\mathrm{vis}}^{95}$ [fb] | 0.63 | 0.55 | 0.26 | 0.36 | 0.24 | 0.26 |
| Expected $\sigma_{\mathrm{vis}}^{95}$ [fb] | $0.78_{-0.23}^{+0.32}$ | $0.62_{-0.18}^{+0.26}$ | $0.37_{-0.11}^{+0.17}$ | $0.30_{-0.09}^{+0.13}$ | $0.24_{-0.08}^{+0.13}$ | $0.19_{-0.06}^{+0.10}$ |

**Table 6**. Observed and expected numbers of events in SR-$WW$. Also shown are the one-sided $p_0$ values and the observed and expected 95% CL upper limits, $\sigma_{\mathrm{vis}}^{95}$, on the visible cross-section for non-SM events. The 'Others' category includes non-prompt lepton, $Z/\gamma^* +$ jets and SM Higgs. The numbers of signal events are shown for the $\tilde{\chi}_1^+ \tilde{\chi}_1^- \rightarrow W^+ \tilde{\chi}_1^0 W^- \tilde{\chi}_1^0$ scenario with different $\tilde{\chi}_1^\pm$ and $\tilde{\chi}_1^0$ masses in GeV.

| | SR-$WW$a | | SR-$WW$b | | SR-$WW$c | |
| --- | --- | --- | --- | --- | --- | --- |
| | SF | DF | SF | DF | SF | DF |
| Background | | | | | | |
| $WW$ | $57.8 \pm 5.5$ | $58.2 \pm 6.0$ | $16.4 \pm 2.5$ | $12.3 \pm 2.0$ | $10.4 \pm 2.7$ | $7.3 \pm 1.9$ |
| $ZV$ | $16.3 \pm 3.5$ | $1.8 \pm 0.5$ | $10.9 \pm 1.9$ | $0.6 \pm 0.2$ | $9.2 \pm 2.1$ | $0.4 \pm 0.2$ |
| Top | $9.2 \pm 3.5$ | $11.6 \pm 4.3$ | $2.4 \pm 1.7$ | $4.3 \pm 1.6$ | $0.6_{-0.6}^{+1.2}$ | $0.9 \pm 0.8$ |
| Others | $3.3 \pm 1.5$ | $2.0 \pm 1.1$ | $0.5 \pm 0.4$ | $0.9 \pm 0.6$ | $0.1_{-0.1}^{+0.5}$ | $0.4 \pm 0.3$ |
| Total | $86.5 \pm 7.4$ | $73.6 \pm 7.9$ | $30.2 \pm 3.5$ | $18.1 \pm 2.6$ | $20.3 \pm 3.5$ | $9.0 \pm 2.2$ |
| Observed events | 73 | 70 | 26 | 17 | 10 | 11 |
| Predicted signal | | | | | | |
| $(m_{\tilde{\chi}_1^\pm}, m_{\tilde{\chi}_1^0}) = (100, 0)$ | $25.6 \pm 3.3$ | $24.4 \pm 2.2$ | | | | |
| $(m_{\tilde{\chi}_1^\pm}, m_{\tilde{\chi}_1^0}) = (140, 20)$ | | | $8.3 \pm 0.8$ | $7.2 \pm 0.8$ | | |
| $(m_{\tilde{\chi}_1^\pm}, m_{\tilde{\chi}_1^0}) = (200, 0)$ | | | | | $5.2 \pm 0.5$ | $4.6 \pm 0.4$ |
| $p_0$ | 0.50 | 0.50 | 0.50 | 0.50 | 0.50 | 0.31 |
| Observed $\sigma_{\mathrm{vis}}^{95}$ [fb] | 0.78 | 1.00 | 0.54 | 0.49 | 0.29 | 0.50 |
| Expected $\sigma_{\mathrm{vis}}^{95}$ [fb] | $1.13_{-0.32}^{+0.46}$ | $1.11_{-0.31}^{+0.44}$ | $0.66_{-0.20}^{+0.28}$ | $0.53_{-0.16}^{+0.23}$ | $0.52_{-0.16}^{+0.23}$ | $0.41_{-0.12}^{+0.19}$ |

**Table 7**. Observed and expected numbers of events in SR-$Z$jets. Also shown are the one-sided $p_0$ value and the observed and expected 95% CL upper limits, $\sigma^{95}_{\mathrm{vis}}$, on the visible cross-section for non-SM events. The numbers of signal events are shown for the $\tilde{\chi}^\pm_1 \tilde{\chi}^0_2 \to W^\pm \tilde{\chi}^0_1 Z \tilde{\chi}^0_1$ scenario with different $\tilde{\chi}^\pm_1$, $\tilde{\chi}^0_2$ and $\tilde{\chi}^0_1$ masses in GeV.

|  | SR-$Z$jets |
|---|---|
| Background |  |
| $\quad WW$ | $0.1 \pm 0.1$ |
| $\quad ZV$ | $1.0 \pm 0.6$ |
| $\quad$ Top | $< 0.1$ |
| $\quad Z + $ jets and others | $0.3 \pm 0.2$ |
| Total | $1.4 \pm 0.6$ |
| Observed events | 1 |
| Predicted signal |  |
| $(m_{\tilde{\chi}^0_2, \tilde{\chi}^\pm_1}, m_{\tilde{\chi}^0_1}) = (250, 0)$ | $6.4 \pm 0.8$ |
| $(m_{\tilde{\chi}^0_2, \tilde{\chi}^\pm_1}, m_{\tilde{\chi}^0_1}) = (350, 50)$ | $3.7 \pm 0.2$ |
| $p_0$ | 0.50 |
| Observed $\sigma^{95}_{\mathrm{vis}}$ [fb] | 0.17 |
| Expected $\sigma^{95}_{\mathrm{vis}}$ [fb] | $0.19^{+0.11}_{-0.06}$ |
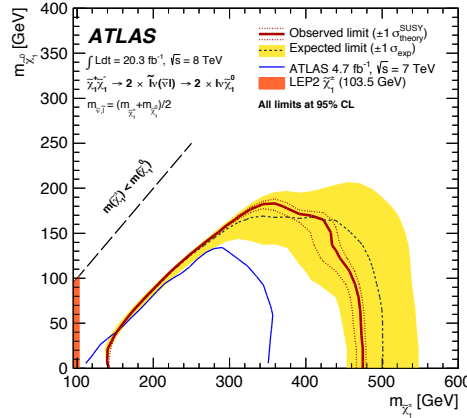


**Figure 5**. Observed and expected 95% CL exclusion regions in the $m_{\tilde{\chi}^\pm_1} - m_{\tilde{\chi}^0_1}$ plane for simplified-model $\tilde{\chi}^+_1 \tilde{\chi}^-_1$ pair production with common masses of sleptons and sneutrinos at $m_{\tilde{\ell}} = m_{\tilde{\nu}} = (m_{\tilde{\chi}^\pm_1} + m_{\tilde{\chi}^0_1})/2$. Also shown is the LEP limit [36] on the mass of the chargino. The blue line indicates the limit from the previous analysis with the 7 TeV data [34].

model for direct $\tilde{\chi}^+_1 \tilde{\chi}^-_1$ pair production followed by slepton-mediated decays. For $m_{\tilde{\chi}^0_1} = 0$, chargino masses between 140 GeV and 465 GeV are excluded. The exclusion in this scenario depends on the assumed slepton mass, which is chosen to be halfway between the $\tilde{\chi}^\pm_1$ and $\tilde{\chi}^0_1$ masses in this analysis. Studies performed with particle-level signal MC samples show that the signal acceptance in SR-$m_{\mathrm{T2}}$ depends weakly on $m_{\tilde{\ell}}$, and the choice of $m_{\tilde{\ell}} = (m_{\tilde{\chi}^\pm_1} + m_{\tilde{\chi}^0_1})/2$ minimizes (maximizes) the acceptance for small (large) $\tilde{\chi}^\pm_1 - \tilde{\chi}^0_1$ mass splitting.
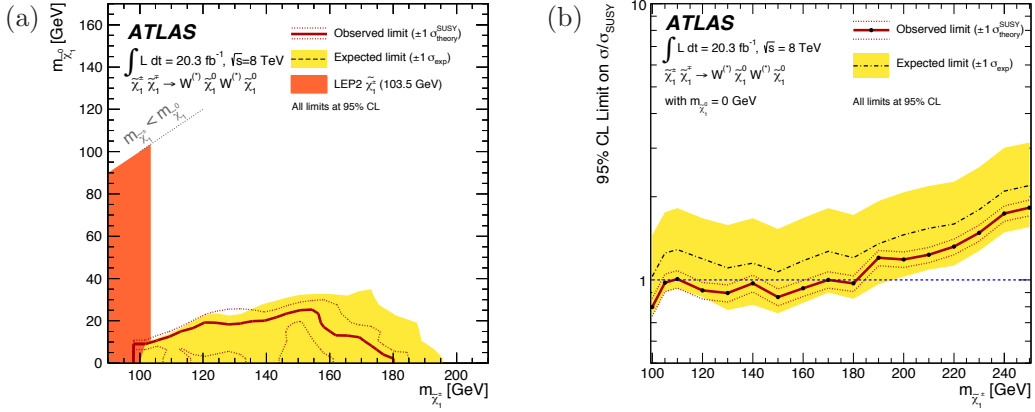
**Figure 6**. (a) Observed and expected 95% CL exclusion regions in the $m_{\tilde{\chi}_1^0}$–$m_{\tilde{\chi}_1^\pm}$ plane for simplified-model $\tilde{\chi}_1^+ \tilde{\chi}_1^-$ production followed by $W$-mediated decays. Also shown is the LEP limit [36] on the mass of the chargino. (b) Observed and expected 95% CL upper limits on the cross-section normalized by the simplified-model prediction as a function of $m_{\tilde{\chi}_1^\pm}$ for $m_{\tilde{\chi}_1^0} = 0$.

Figure 6(a) shows the 95% CL exclusion regions obtained from SR-$WW$ on the simplified-model $\tilde{\chi}_1^+ \tilde{\chi}_1^-$ production followed by $W$-mediated decays. Figure 6(b) shows the observed and expected 95% CL upper limits on the SUSY signal cross-section normalized by the simplified-model prediction as a function of $m_{\tilde{\chi}_1^\pm}$ for a massless $\tilde{\chi}_1^0$. For $m_{\tilde{\chi}_1^0} = 0$, chargino mass ranges of 100–105 GeV, 120–135 GeV and 145–160 GeV are excluded at 95% CL.

Figure 7(a) shows the 95% CL exclusion region obtained from SR-$Z$jets in the simplified-model $\tilde{\chi}_1^\pm \tilde{\chi}_2^0$ production followed by $W$ and $Z$ decays. For $m_{\tilde{\chi}_1^0} = 0$, degenerate $\tilde{\chi}_1^\pm$ and $\tilde{\chi}_2^0$ masses between 180 GeV and 355 GeV are excluded. Figure 7(b) shows the exclusion region obtained by combining this result with results from the relevant signal regions (SR0a/SR1a/SR1SS/SR2a) in the ATLAS search for electroweak SUSY production in the three-lepton final states [82]. The fit is performed on the combined likelihood function using all signal regions. The uncertainties are profiled in the likelihood and correlations between channels and processes are taken into account. The combination significantly improves the sensitivity. As a result, degenerate $\tilde{\chi}_1^\pm$ and $\tilde{\chi}_2^0$ masses between 100 GeV and 415 GeV are excluded at 95% CL for $m_{\tilde{\chi}_1^0} = 0$.

Figure 8 shows the 95% CL exclusion regions obtained from SR-$m_{\text{T2}}$ for the direct production of (a) right-handed, (b) left-handed, and (c) both right- and left-handed selectrons and smuons of equal mass in the $m_{\tilde{\chi}_1^0}$–$m_{\tilde{\ell}}$ plane. For $m_{\tilde{\chi}_1^0} = 0$, common values for left and right-handed selectron and smuon mass between 90 GeV and 325 GeV are excluded. The sensitivity decreases as the $\tilde{\ell}$–$\tilde{\chi}_1^0$ mass splitting decreases because the $m_{\text{T2}}$ end point of the SUSY signal moves lower towards that of the SM background. For $m_{\tilde{\chi}_1^0} = 100$ GeV, common left and right-handed slepton masses between 160 GeV and 310 GeV are excluded. The present result cannot be directly compared with the previous ATLAS slepton limits [34], which used a flavour-blind signal region and searched for a single slepton flavour with both right-handed and left-handed contributions.
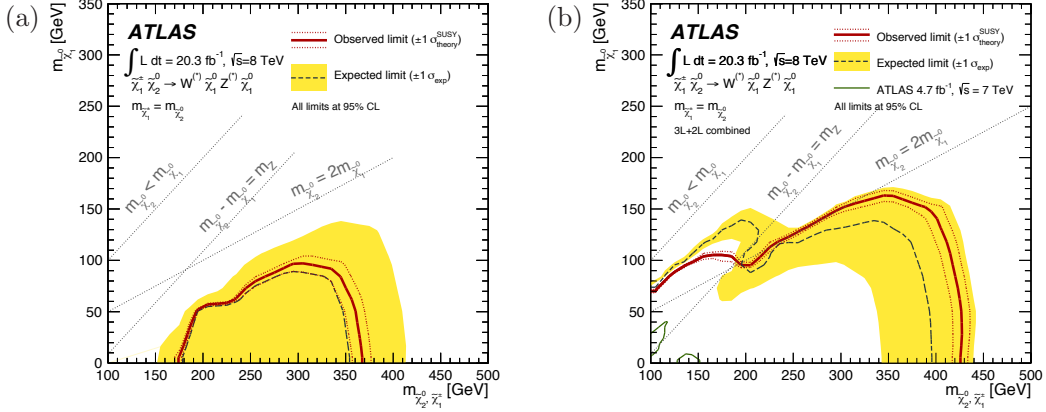
**Figure 7**. (a) Observed and expected 95% CL exclusion regions in the $m_{\tilde{\chi}_2^0,\tilde{\chi}_1^\pm}-m_{\tilde{\chi}_1^0}$ plane for simplified-model $\tilde{\chi}_1^\pm \tilde{\chi}_2^0$ production followed by $W$ and $Z$-mediated decays obtained from SR-$Z$jets; and (b) the exclusion regions obtained by combining with the ATLAS three-lepton search [82]. The green lines in (b) indicate the regions excluded by ATLAS using 4.7 fb$^{-1}$ of $\sqrt{s} = 7$ TeV data [104].

Figure 9(a)–(c) show the 95% CL exclusion regions in the pMSSM $\mu - M_2$ plane for the scenario with right-handed sleptons with $m_{\tilde{\ell}_R} = (m_{\tilde{\chi}_1^0} + m_{\tilde{\chi}_2^0})/2$. The $M_1$ parameter is set to (a) 100 GeV, (b) 140 GeV and (c) 250 GeV, and $\tan\beta = 6$. At each model point, the limits are obtained using the SR with the best expected sensitivity. Fig. 9(d) shows the exclusion region for $M_1 = 250$ GeV obtained by combining the results of this analysis with the ATLAS three-lepton results [82]. Figure 10(a) shows the 95% CL exclusion region in the pMSSM $\mu - M_2$ plane for the scenario with heavy sleptons, $\tan\beta = 10$ and $M_1 = 50$ GeV, using the SR with the best expected sensitivity at each model point. The island of exclusion near the centre of figure 10(a) is due to SR-$Z$jets, and is shaped by the kinematical thresholds of the $\tilde{\chi}_1^\pm \to W\tilde{\chi}_1^0$ and $\tilde{\chi}_2^0 \to Z\tilde{\chi}_1^0$ decays. Figure 10(b) shows the exclusion region obtained by combining the results from SR-$Z$jets with the three-lepton results. These results significantly extend previous limits in the pMSSM $\mu - M_2$ plane.

The CL$_s$ value is also calculated from SR-$WW$a for the GMSB model point where the chargino is the NLSP with $m_{\tilde{\chi}_1^\pm} = 110$ GeV, $m_{\tilde{\chi}_1^0} = 113$ GeV and $m_{\tilde{\chi}_2^0} = 130$ GeV [46]. The observed and expected CL$_s$ values are found to be 0.19 and 0.29, respectively. The observed and expected 95% CL limits on the signal cross-section are 1.58 and 1.90 times the model prediction, respectively.

## 11 Conclusion

Searches for the electroweak production of charginos, neutralinos and sleptons in final states characterized by the presence of two leptons (electrons and muons) and missing transverse momentum are performed using 20.3 fb$^{-1}$ of proton-proton collision data at $\sqrt{s} = 8$ TeV recorded with the ATLAS experiment at the Large Hadron Collider. No significant excess beyond Standard Model expectations is observed. Limits are set on the masses of the
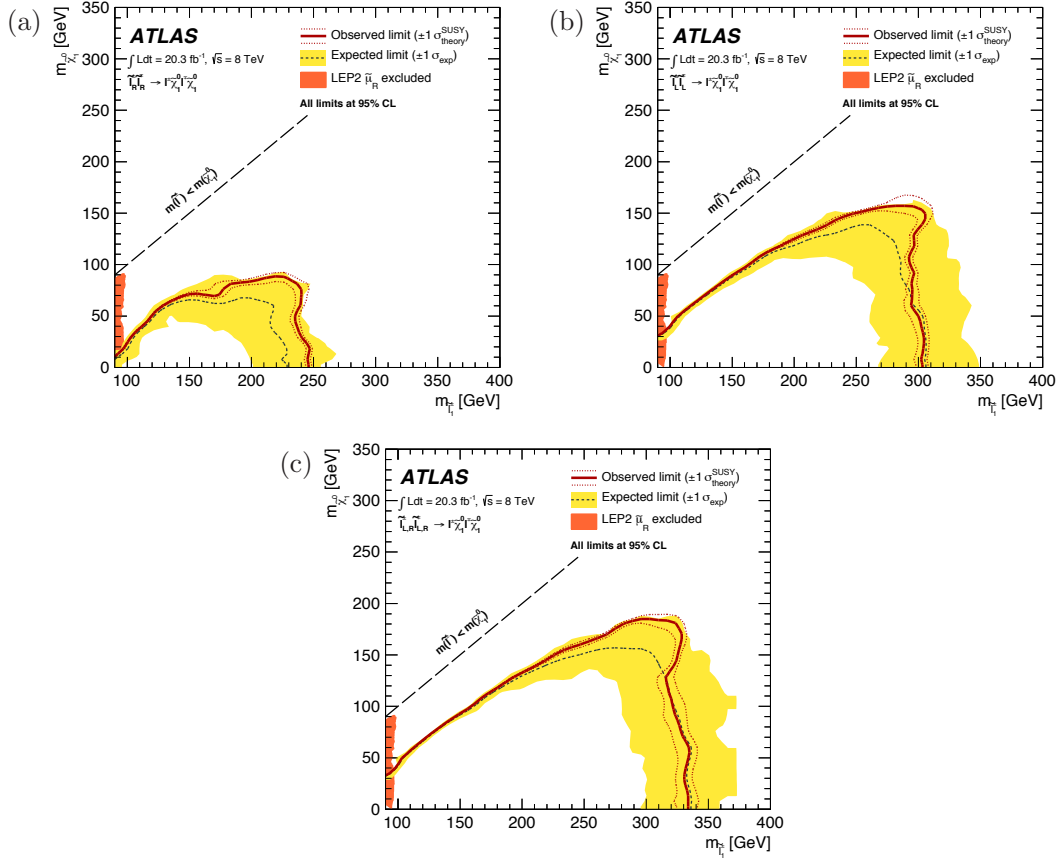
**Figure 8**. 95% CL exclusion regions in the $m_{\tilde{\chi}_1^0}$–$m_{\tilde{\ell}}$ plane for (a) right-handed, (b) left-handed, and (c) both right- and left-handed (mass degenerate) selectron and smuon production. Also illustrated are the LEP limits [36] on the mass of the right-handed smuon $\tilde{\mu}_R$.

lightest chargino $\tilde{\chi}_1^\pm$, next-to-lightest neutralino $\tilde{\chi}_2^0$ and sleptons for different masses of the lightest neutralino $\tilde{\chi}_1^0$ in simplified models. In the scenario of $\tilde{\chi}_1^+\tilde{\chi}_1^-$ pair production with $\tilde{\chi}_1^\pm$ decaying into $\tilde{\chi}_1^0$ via an intermediate slepton with mass halfway between the $\tilde{\chi}_1^\pm$ and $\tilde{\chi}_1^0$, $\tilde{\chi}_1^\pm$ masses between 140 GeV and 465 GeV are excluded at 95% CL for a massless $\tilde{\chi}_1^0$. In the scenario of $\tilde{\chi}_1^+\tilde{\chi}_1^-$ pair production with $\tilde{\chi}_1^\pm$ decaying into $\tilde{\chi}_1^0$ and a $W$ boson, $\tilde{\chi}_1^\pm$ masses in the ranges 100–105 GeV, 120–135 GeV and 145–160 GeV are excluded at 95% CL for a massless $\tilde{\chi}_1^0$. This is the first limit for this scenario obtained at a hadron collider. Finally, in the scenario of $\tilde{\chi}_1^\pm\tilde{\chi}_2^0$ production with $\tilde{\chi}_1^\pm$ decaying into $W\tilde{\chi}_1^0$ and $\tilde{\chi}_2^0$ decaying into $Z\tilde{\chi}_1^0$, common $\tilde{\chi}_1^\pm$ and $\tilde{\chi}_2^0$ masses between 180 GeV and 355 GeV are excluded at 95% CL for a massless $\tilde{\chi}_1^0$. Combining this result with those from ref. [82] extends the exclusion region to between 100 GeV and 415 GeV. In scenarios where sleptons decay directly into $\tilde{\chi}_1^0$ and a charged lepton, common values for left and right-handed slepton masses between 90 GeV and 325 GeV are excluded at 95% CL for a massless $\tilde{\chi}_1^0$. Improved exclusion regions are also obtained in the pMSSM $\mu$–$M_2$ plane for four sets of slepton mass, $M_1$ and $\tan\beta$
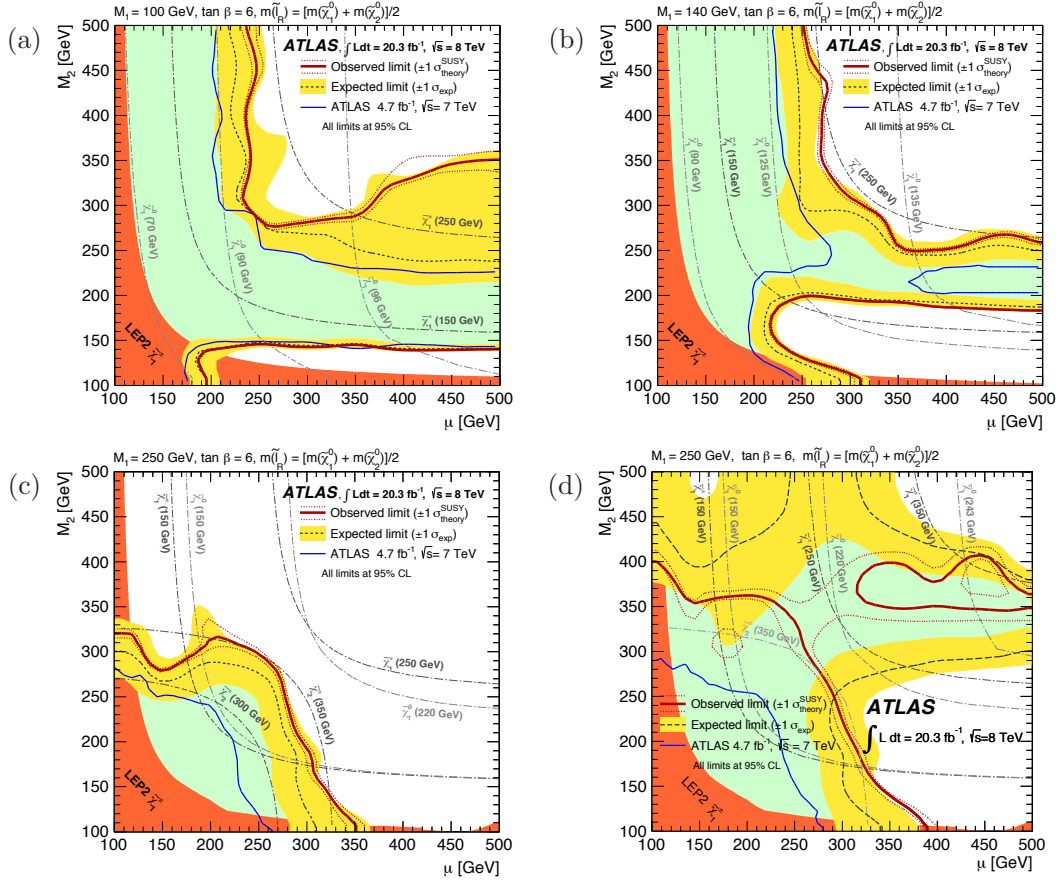
**Figure 9**. 95% CL exclusion regions in the $\mu$–$M_2$ mass plane of the pMSSM with right-handed slepton mass $m_{\tilde{\ell}_R} = (m_{\tilde{\chi}_1^0} + m_{\tilde{\chi}_2^0})/2$. The areas covered by the $-1\sigma$ expected limit are shown in green. The $M_1$ parameter is (a) 100 GeV, (b) 140 GeV and (c) 250 GeV, and $\tan\beta = 6$. The exclusion region for $M_1 = 250$ GeV (d) is obtained by combining the results of this analysis with those from the ATLAS three-lepton search [82]. The dash-dotted lines indicate the masses of $\tilde{\chi}_1^\pm$ and $\tilde{\chi}_1^0$. Also shown are the previously reported exclusion regions by ATLAS [104] and the LEP limits [36] on the mass of the chargino.

values.

## 12 Acknowledgements
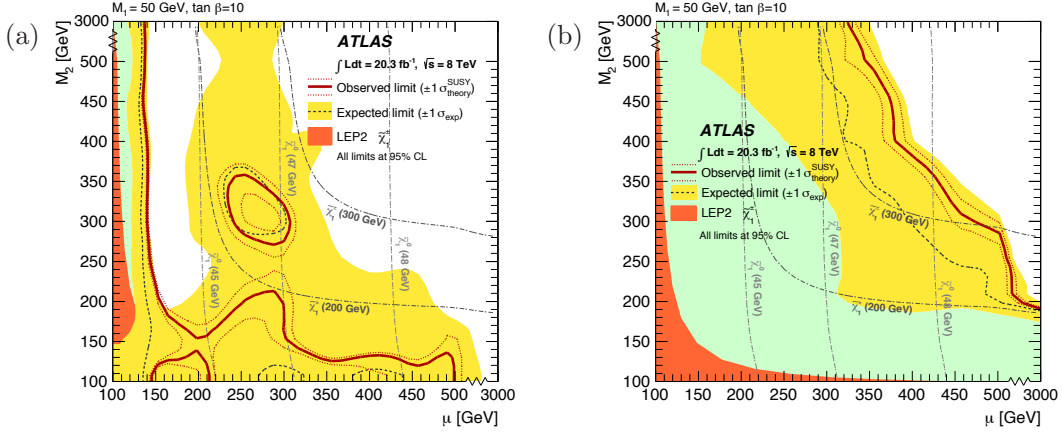
**Figure 10**. (a) 95% CL exclusion regions in the $\mu$–$M_2$ mass plane of the pMSSM with very large slepton masses, $M_1 = 50$ GeV and $\tan\beta = 10$. (b) The exclusion region obtained by combining the results form SR-$Z$jets with those from the ATLAS three-lepton search [82]. The areas covered by the $-1\sigma$ expected limit are shown in green. The dash-dotted lines indicate the masses of $\tilde{\chi}_1^\pm$ and $\tilde{\chi}_1^0$. Also shown are the LEP limits [36] on the mass of the chargino.

# References

[1] H. Miyazawa, *Baryon Number Changing Currents*, *Prog. Theor. Phys.* **36 (6)** (1966) 1266.

[2] P. Ramond, *Dual Theory for Free Fermions*, *Phys. Rev.* **D3** (1971) 2415.

[3] Y. A. Gol'fand and E. P. Likhtman, *Extension of the Algebra of Poincare Group Generators and Violation of P Invariance*, *JETP Lett.* **13** (1971) 323. [Pisma Zh. Eksp. Teor. Fiz. **13** (1971) 452].

[4] A. Neveu and J. H. Schwarz, *Factorizable dual model of pions*, *Nucl. Phys.* **B31** (1971) 86.

[5] A. Neveu and J. H. Schwarz, *Quark Model of Dual Pions*, *Phys. Rev.* **D4** (1971) 1109.

[6] J. Gervais and B. Sakita, *Field theory interpretation of supergauges in dual models*, *Nucl. Phys.* **B34** (1971) 632.

[7] D. V. Volkov and V. P. Akulov, *Is the Neutrino a Goldstone Particle?*, *Phys. Lett.* **B46** (1973) 109.

[8] J. Wess and B. Zumino, *A Lagrangian Model Invariant Under Supergauge Transformations*, *Phys. Lett.* **B49** (1974) 52.

[9] J. Wess and B. Zumino, *Supergauge Transformations in Four-Dimensions*, *Nucl. Phys.* **B70** (1974) 39.

[10] S. Weinberg, *Implications of Dynamical Symmetry Breaking*, *Phys. Rev.* **D13** (1976) 974.

[11] E. Gildener, *Gauge Symmetry Hierarchies*, *Phys. Rev.* **D14** (1976) 1667.

[12] S. Weinberg, *Implications of Dynamical Symmetry Breaking: An Addendum*, *Phys. Rev.* **D19** (1979) 1277.

[13] L. Susskind, *Dynamics of Spontaneous Symmetry Breaking in the Weinberg-Salam Theory*, *Phys. Rev.* **D20** (1979) 2619.

[14] P. Fayet, *Supersymmetry and Weak, Electromagnetic and Strong Interactions*, *Phys. Lett.* **B64** (1976) 159.

[15] P. Fayet, *Spontaneously Broken Supersymmetric Theories of Weak, Electromagnetic and Strong Interactions*, *Phys. Lett.* **B69** (1977) 489.

[16] G. R. Farrar and P. Fayet, *Phenomenology of the Production, Decay, and Detection of New Hadronic States Associated with Supersymmetry*, *Phys. Lett.* **B76** (1978) 575.

[17] P. Fayet, *Relations Between the Masses of the Superpartners of Leptons and Quarks, the Goldstino Couplings and the Neutral Currents*, *Phys. Lett.* **B84** (1979) 416.

[18] S. Dimopoulos and H. Georgi, *Softly Broken Supersymmetry and SU(5)*, *Nucl. Phys.* **B193** (1981) 150.

[19] A. Djouadi, J.-L. Kneur, and G. Moultaka, *SuSpect: A Fortran code for the supersymmetric and Higgs particle spectrum in MSSM*, *Comput. Phys. Commun.* **176** (2007) 426, [`hep-ph/0211331`].

[20] C. F. Berger, J. S. Gainer, J. L. Hewett, and T. G. Rizzo, *Supersymmetry Without Prejudice*, *JHEP* **02** (2009) 023, [`hep-ph/0211331`].

[21] S. S. AbdusSalam et al., *Fitting the Phenomenological MSSM*, *Phys. Rev.* **D81** (2010) 095012, [`arXiv:0904.2548`].

[22] R. Barbieri and G. F. Giudice, *Upper Bounds on Supersymmetric Particle Masses*, *Nucl. Phys.* **B306** (1988) 63.

[23] B. de Carlos and J. A. Casas, *One loop analysis of the electroweak breaking in supersymmetric models and the fine tuning problem*, *Phys. Lett.* **B309** (1993) 320, [`hep-ph/9303291`].

[24] M. Dine and W. Fischler, *A Phenomenological Model of Particle Physics Based on Supersymmetry*, *Phys. Lett.* **B110** (1982) 227.

[25] L. Alvarez-Gaume, M. Claudson, and M. B. Wise, *Low-Energy Supersymmetry*, *Nucl. Phys.* **B207** (1982) 96.

[26] C. R. Nappi and B. A. Ovrut, *Supersymmetric Extension of the SU(3) × SU(2) × U(1) Model*, *Phys. Lett.* **B113** (1982) 175.

[27] M. Dine and A. E. Nelson, *Dynamical supersymmetry breaking at low-energies*, *Phys. Rev.* **D48** (1993) 1277, [`hep-ph/9303230`].

[28] M. Dine, A. E. Nelson, and Y. Shirman, *Low-energy dynamical supersymmetry breaking simplified*, *Phys. Rev.* **D51** (1995) 1362, [`hep-ph/9408384`].

[29] M. Dine, A. E. Nelson, Y. Nir, and Y. Shirman, *New tools for low-energy dynamical supersymmetry breaking*, *Phys. Rev.* **D53** (1996) 2658, [`hep-ph/9507378`].

[30] L. Randall and R. Sundrum, *Out of this world supersymmetry breaking*, *Nucl. Phys.* **B557** (1999) 79, [`hep-th/9810155`].

[31] G. F. Giudice, M. A. Luty, H. Murayama, and R. Rattazzi, *Gaugino mass without singlets*, *JHEP* **12** (1998) 027, [`hep-ph/9810442`].

[32] G. Belanger, F. Boudjema, A. Cottrant, A. Pukhov, and A. Semenov, *WMAP constraints on SUGRA models with non-universal gaugino masses and prospects for direct detection*, *Nucl. Phys.* **B706** (2005) 411, [`hep-ph/0407218`].

[33] S. King, J. Roberts, and D. Roy, *Natural dark matter in SUSY GUTs with non-universal gaugino masses*, *JHEP* **10** (2007) 106, [`arXiv:0705.4219`].

[34] **ATLAS** Collaboration, *Search for direct slepton and gaugino production in final states with two leptons and missing transverse momentum with the ATLAS detector in pp collisions at $\sqrt{s} = 7$ TeV*, *Phys. Lett.* **B718** (2013) 879, [`arXiv:1208.2884`].

[35] **CMS** Collaboration, *Search for electroweak production of charginos and neutralinos using leptonic final states in pp collisions at $\sqrt{s} = 7$ TeV*, *JHEP* **11** (2012) 147, [`arXiv:1209.6620`].

[36] LEP SUSY Working Group (ALEPH, DELPHI, L3, OPAL). Notes LEPSUSYWG/01-03.1, 04-01.1, `http://lepsusy.web.cern.ch/lepsusy/Welcome.html`.

[37] **ALEPH** Collaboration, A. Heister et al., *Absolute mass lower limit for the lightest neutralino of the MSSM from $e^+e^-$ data at $\sqrt{s}$ up to 209 GeV*, *Phys. Lett.* **B583** (2004) 247.

[38] **DELPHI** Collaboration, J. Abdallah et al., *Searches for supersymmetric particles in $e^+e^-$ collisions up to 208 GeV and interpretation of the results within the MSSM*, *Eur. Phys. J.* **C31** (2003) 421, [`hep-ex/0311019`].

[39] **L3** Collaboration, M. Acciarri et al., *Search for charginos and neutralinos in $e^+e^-$ collisions at $\sqrt{s} = 189$ GeV*, *Phys. Lett.* **B472** (2000) 420, [`hep-ex/9910007`].

[40] **OPAL** Collaboration, G. Abbiendi et al., *Search for chargino and neutralino production at $\sqrt{s} = 192$ GeV to 209 GeV at LEP*, *Eur. Phys. J.* **C35** (2004) 1, [`hep-ex/0401026`].

[41] J. Alwall, P. Schuster, and N. Toro, *Simplified Models for a First Characterization of New Physics at the LHC*, *Phys. Rev.* **D79** (2009) 075020, [`arXiv:0810.3921`].

[42] S. AbdusSalam et al., *Benchmark Models, Planes, Lines and Points for Future SUSY Searches at the LHC*, *Eur. Phys. J.* **C71** (2011) 1835, [`arXiv:1109.3859`].

[43] A. Djouadi et al., *The Minimal supersymmetric standard model: Group summary report*, `hep-ph/9901246`.

[44] **ATLAS** Collaboration, *Observation of a new particle in the search for the Standard Model Higgs boson with the ATLAS detector at the LHC*, Phys. Lett. **B716** (2012) 1, [arXiv:1207.7214].

[45] **CMS** Collaboration, *Observation of a new boson at a mass of 125 GeV with the CMS experiment at the LHC*, Phys. Lett. **B716** (2012) 30, [arXiv:1207.7235].

[46] D. Curtin, P. Jaiswal, and P. Meade, *Charginos Hiding In Plain Sight*, Phys. Rev. **D87** (2013) 031701, [arXiv:1206.6888].

[47] **ATLAS** Collaboration, *The ATLAS Experiment at the CERN Large Hadron Collider*, JINST **3** (2008) S08003.

[48] **GEANT4** Collaboration, S. Agostinelli et al., *GEANT4: A simulation toolkit*, Nucl. Instrum. Meth. **A506** (2003) 250.

[49] **ATLAS** Collaboration, *The ATLAS Simulation Infrastructure*, Eur. Phys. J. **C70** (2010) 823, [arXiv:1005.4568].

[50] E. Richter-Was, D. Froidevaux, and L. Poggioli, *ATLFAST 2.0 a fast simulation package for ATLAS*, ATL-PHYS-98-131, http://cds.cern.ch/record/683751.

[51] **ATLAS** Collaboration, *The simulation principle and performance of the ATLAS fast calorimeter simulation FastCaloSim*, ATL-PHYS-PUB-2010-013, http://cds.cern.ch/record/1300517.

[52] T. Sjostrand, S. Mrenna, and P. Skands, *PYTHIA 6.4 physics and manual*, JHEP **05** (2006) 026, [hep-ph/0603175].

[53] S. Frixione and B. R. Webber, *Matching NLO QCD computations and parton shower simulations*, JHEP **06** (2002) 029.

[54] S. Frixione, P. Nason, and B. R. Webber, *Matching NLO QCD and parton showers in heavy flavour production*, JHEP **08** (2003) 007.

[55] S. Frixione, E. Laenen, P. Motylinski, and B. R. Webber, *Single-top production in MC@NLO*, JHEP **03** (2006) 092.

[56] S. Frixione, P. Nason, and C. Oleari, *Matching NLO QCD computations with Parton Shower similations: the POWHEG method*, JHEP **11** (2007) 070.

[57] B. P. Kersevan and E. Richter-Was, *The Monte Carlo event generator AcerMC version 2.0 to 3.8 with interfaces to PYTHIA 6.4, HERWIG 6.5 and ARIADNE 4.1*, Comp. Phys. Comm. **184** (2013) 919, [hep-ph/0405247].

[58] M. Czakon and A. Mitov, *Top++: A Program for the Calculation of the Top-Pair Cross-Section at Hadron Colliders*, arXiv:1112.5675.

[59] J. Alwall, M. Herquet, F. Maltoni, O. Mattelaer, and T. Stelzer, *MadGraph 5 : Going Beyond*, JHEP **06** (2011) 128, [arXiv:1106.0522].

[60] A. Lazopoulos, T. McElmurry, K. Melnikov, and F. Petriello, *Next-to-leading order QCD corrections to $t\bar{t}Z$ production at the LHC*, Phys. Lett. **B666** (2008) 62, [arXiv:0804.2220].

[61] J. M. Campbell and R. K. Ellis, *$t\bar{t}W^{\pm}$ production and decay at NLO*, JHEP **07** (2012) 052, [arXiv:1204.5678].

[62] M. Garzelli, A. Kardos, C. Papadopoulos, and Z. Trocsanyi, *$t\bar{t}\,W^{\pm}$ and $t\bar{t}\,Z$ hadroproduction at NLO accuracy in QCD with parton shower and hadronization effects*, JHEP **11** (2012) 056, [arXiv:1208.2665].

[63] T. Binoth, M. Ciccolini, N. Kauer, and M. Kramer, *Gluon-induced W-boson pair production at the LHC*, *JHEP* **12** (2006) 046, [hep-ph/0611170].

[64] T. Binoth, N. Kauer, and P. Mertsch, *Gluon-induced QCD corrections to $pp \to ZZ \to \ell\bar{\ell}\ell'\bar{\ell}'$*, arXiv:0807.0024.

[65] P. Artoisenet et al., *A framework for Higgs characterisation*, *JHEP* **11** (2013) 043, [arXiv:1306.6464].

[66] J. M. Campbell and R. K. Ellis, *An Update on vector boson pair production at hadron colliders*, *Phys. Rev.* **D60** (1999) 113006, [hep-ph/9905386].

[67] J. M. Campbell, R. K. Ellis, and C. Williams, *Vector boson pair production at the LHC*, *JHEP* **07** (2011) 018, [arXiv:1105.0020].

[68] F. Campanario, V. Hankele, C. Oleari, S. Prestel, and D. Zeppenfeld, *QCD corrections to charged triple vector boson production with leptonic decay*, *Phys. Rev.* **D78** (2008) 094012, [arXiv:0809.0790].

[69] T. Gleisberg et al., *Event generation with SHERPA 1.1*, *JHEP* **02** (2009) 007, [arXiv:0811.4622].

[70] M. L. Mangano, M. Moretti, F. Piccinini, R. Pittau, and A. D. Polosa, *ALPGEN, a generator for hard multiparton processes in hadronic collisions*, *JHEP* **07** (2003) 001, [hep-ph/0206293].

[71] S. Catani, L. Cieri, G. Ferrera, D. de Florian, and M. Grazzini, *Vector boson production at hadron colliders: A Fully exclusive QCD calculation at NNLO*, *Phys. Rev. Lett.* **103** (2009) 082001, [arXiv:0903.2120].

[72] G. Corcella et al., *HERWIG 6: An event generator for hadron emission reactions with interfering gluons (including supersymmetric processes)*, *JHEP* **01** (2001) 010, [hep-ph/0011363].

[73] J. M. Butterworth, J. R. Forshaw, and M. H. Seymour, *Multiparton interactions in photoproduction at HERA*, *Z. Phys.* **C72** (1996) 637, [hep-ph/9601371].

[74] **ATLAS** Collaboration, *ATLAS tunes of PYTHIA 6 and Pythia 8 for MC11*, ATL-PHYS-PUB-2011-009, http://cds.cern.ch/record/1363300.

[75] H.-L. Lai et al., *New parton distributions for collider physics*, *Phys. Rev.* **D82** (2010) 074024, [arXiv:1007.2241].

[76] J. Pumplin et al., *New generation of parton distributions with uncertainties from global QCD analysis*, *JHEP* **07** (2002) 012, [hep-ph/0201195].

[77] M. Bahr et al., *Herwig++ Physics and Manual*, *Eur. Phys. J.* **C58** (2008) 639, [arXiv:0803.0883].

[78] W. Beenakker et al., *The Production of charginos/neutralinos and sleptons at hadron colliders*, *Phys. Rev. Lett.* **83** (1999) 3780, [hep-ph/9906298].

[79] B. Fuks, M. Klasen, D. R. Lamprea, and M. Rothering, *Gaugino production in proton-proton collisions at a center-of-mass energy of 8 TeV*, *JHEP* **10** (2012) 081, [arXiv:1207.2159].

[80] B. Fuks, M. Klasen, D. R. Lamprea, and M. Rothering, *Precision predictions for electroweak superpartner production at hadron colliders with Resummino*, *Eur. Phys. J.* **C73** (2013) 2480, [arXiv:1304.0790].

[81] B. Fuks, M. Klasen, D. R. Lamprea, and M. Rothering, *Revisiting slepton pair production at the Large Hadron Collider*, *JHEP* **01** (2014) 168, [arXiv:1310.2621].

[82] **ATLAS** Collaboration, *Search for direct production of charginos and neutralinos in events with three leptons and missing transverse momentum in $\sqrt{s} = 8$ TeV pp collisions with the ATLAS detector*, *Submitted to JHEP* [arXiv:1402.7029].

[83] **ATLAS** Collaboration, *Electron performance measurements with the ATLAS detector using the 2010 LHC proton-proton collision data*, *Eur. Phys. J.* **C72** (2012) 1909, [arXiv:1110.3174].

[84] **ATLAS** Collaboration, *Preliminary results on the muon reconstruction efficiency, momentum resolution, and momentum scale in ATLAS 2012 pp collision data*, ATLAS-CONF-2013-088, http://cdsweb.cern.ch/record/1580207.

[85] M. Cacciari, G. P. Salam, and G. Soyez, *The anti-$k_t$ jet clustering algorithm*, *JHEP* **04** (2008) 063, [arXiv:0802.1189].

[86] M. Cacciari and G. P. Salam, *Dispelling the $N^3$ myth for the $k_t$ jet-finder*, *Phys. Lett.* **B641** (2006) 57, [hep-ph/0512210].

[87] **ATLAS** Collaboration, *Jet energy measurement with the ATLAS detector in proton-proton collisions at $\sqrt{s} = 7$ TeV*, *Eur. Phys. J.* **C73** (2013) 2304, [arXiv:1112.6426].

[88] M. Cacciari, G. P. Salam, and G. Soyez, *The Catchment Area of Jets*, *JHEP* **04** (2008) 005, [arXiv:0802.1188].

[89] **ATLAS** Collaboration, *Commissioning of the ATLAS high-performance b-tagging algorithms in the 7 TeV collision data*, ATLAS-CONF-2011-102, http://cdsweb.cern.ch/record/1369219.

[90] **ATLAS** Collaboration, *Identification of hadronic decays of tau leptons in 2012 data with the ATLAS Detector*, ATLAS-CONF-2013-064, http://cdsweb.cern.ch/record/1562839.

[91] **ATLAS** Collaboration, *Determination of the tau energy scale and the associated systematic uncertainty in proton-proton collisions at $\sqrt{s} = 8$ TeV with the ATLAS detector at the LHC in 2012*, ATLAS-CONF-2013-044, http://cds.cern.ch/record/1544036.

[92] **ATLAS** Collaboration, *Performance of Missing Transverse Momentum Reconstruction in Proton-Proton Collisions at 7 TeV with ATLAS*, *Eur. Phys. J.* **C72** (2012) 1844, [arXiv:1108.5602].

[93] C. G. Lester and D. J. Summers, *Measuring masses of semi invisibly decaying particles pair produced at hadron colliders*, *Phys. Lett.* **B463** (1999) 99, [hep-ph/9906349].

[94] A. Barr, C. Lester, and P. Stephens, *$m_{T2}$ : The Truth behind the glamour*, *J. Phys.* **G29** (2003) 2343, [hep-ph/0304226].

[95] **ATLAS** Collaboration, *Measurement of the top quark-pair production cross section with ATLAS in pp collisions at $\sqrt{s} = 7$ TeV*, *Eur. Phys. J.* **C71** (2011) 1577, [arXiv:1012.1792].

[96] **ATLAS** Collaboration, *Jet energy measurement with the ATLAS detector in proton-proton collisions at $\sqrt{s} = 7$ TeV*, *Eur. Phys. J.* **C73** (2013) 2304, [arXiv:1112.6426].

[97] **ATLAS** Collaboration, *Jet energy resolution in proton-proton collisions at $\sqrt{s} = 7$ TeV recorded in 2010 with the ATLAS detector*, *Eur. Phys. J.* **C73** (2013) 2306, [arXiv:1210.6210].

[98]  **ATLAS** Collaboration, *Measuring the b-tag efficiency in a $t\bar{t}$ sample with 4.7 $fb^{-1}$ of data from the ATLAS detector*, ATLAS-CONF-2012-097, http://cds.cern.ch/record/1460443.

[99]  **ATLAS** Collaboration, *Improved luminosity determination in pp collisions at $\sqrt{s} = 7$ TeV using the ATLAS detector at the LHC*, Eur. Phys. J. **C73** (2013) 2518, [arXiv:1302.4393].

[100]  **ATLAS** Collaboration, *Measurement of $t\bar{t}$ production with a veto on additional central jet activity in pp collisions at $\sqrt{s} = 7$ TeV using the ATLAS detector*, Eur. Phys. J. **C72** (2012) 2043, [arXiv:1203.5015].

[101]  M. Kramer et al., *Supersymmetry production cross sections in pp collisions at $\sqrt{s} = 7$ TeV*, arXiv:1206.2892.

[102]  G. Cowan, K. Cranmer, E. Gross, and O. Vitells, *Asymptotic formulae for likelihood-based tests of new physics*, Eur. Phys. J. **C71** (2011) 1554, [arXiv:1007.1727].

[103]  A. L. Read, *Presentation of search results: The $CL_s$ technique*, J. Phys. **G28** (2002) 2693.

[104]  **ATLAS** Collaboration, *Search for direct production of charginos and neutralinos in events with three leptons and missing transverse momentum in $\sqrt{s} = 7$ TeV pp collisions with the ATLAS detector*, Phys. Lett. **B718** (2013) 841, [arXiv:1208.3144].

| $(m_{\tilde{\ell}}, m_{\tilde{\chi}_1^0})$ | (191, 90) GeV | | (250, 10) GeV | |
|---|---|---|---|---|
| Lepton flavour | $e^+e^-$ | $\mu^+\mu^-$ | $e^+e^-$ | $\mu^+\mu^-$ |
| Two signal leptons | 135.4 | 147.8 | 51.2 | 47.0 |
| Jet veto | 60.5 | 64.7 | 19.4 | 19.8 |
| $Z$ Veto | 55.7 | 60.0 | 18.7 | 19.3 |
| SR-$m_{\mathrm{T2}}^{90}$ | 21.8 | 21.7 | 11.7 | 12.3 |
| SR-$m_{\mathrm{T2}}^{120}$ | 8.0 | 8.5 | 9.1 | 10.0 |
| SR-$m_{\mathrm{T2}}^{150}$ | 0.6 | 1.1 | 7.0 | 7.4 |

| $(m_{\tilde{\chi}_1^\pm}, m_{\tilde{\chi}_1^0})$ | (350, 0) GeV | | | (425, 75) GeV | | |
|---|---|---|---|---|---|---|
| Lepton flavour | $e^+e^-$ | $\mu^+\mu^-$ | $e^\pm\mu^\mp$ | $e^+e^-$ | $\mu^+\mu^-$ | $e^\pm\mu^\mp$ |
| Two signal leptons | 52.0 | 47.8 | 77.7 | 20.5 | 19.9 | 31.3 |
| Jet veto | 22.4 | 20.7 | 32.4 | 8.3 | 8.0 | 12.3 |
| $Z$ veto | 21.2 | 19.3 | 32.4 | 7.8 | 7.7 | 12.3 |
| SR-$m_{\mathrm{T2}}^{90}$ | 12.7 | 11.5 | 19.1 | 4.8 | 4.9 | 7.9 |
| SR-$m_{\mathrm{T2}}^{120}$ | 9.4 | 8.7 | 14.7 | 3.8 | 3.9 | 6.3 |
| SR-$m_{\mathrm{T2}}^{150}$ | 6.2 | 5.7 | 10.1 | 2.7 | 3.0 | 4.6 |

| Signal model | S1 | | S2 | |
|---|---|---|---|---|
| Lepton flavour | $e^+e^-$ | $\mu^+\mu^-$ | $e^+e^-$ | $\mu^+\mu^-$ |
| Two signal leptons | 63.2 | 71.0 | 16.3 | 16.4 |
| >1 light jets | 48.7 | 54.6 | 13.1 | 13.2 |
| No $b$- and forward jets | 36.8 | 40.9 | 9.8 | 9.5 |
| $Z$ window | 35.5 | 39.2 | 9.4 | 9.1 |
| $p_{\mathrm{T},\ell\ell} > 80$ GeV | 27.4 | 29.2 | 8.2 | 8.0 |
| $E_{\mathrm{T}}^{\mathrm{miss,rel}} > 80$ GeV | 12.5 | 14.7 | 5.4 | 5.1 |
| $0.3 < \Delta R_{\ell\ell} < 1.5$ | 9.6 | 10.2 | 4.6 | 4.2 |
| $50 < m_{jj} < 100$ GeV | 6.1 | 6.6 | 3.1 | 2.7 |
| Jet $p_{\mathrm{T}} > 45$ GeV | 2.9 | 3.5 | 1.9 | 1.8 |

| Signal model | S1 | | | GMSB | | |
|---|---|---|---|---|---|---|
| Lepton flavour | $e^+e^-$ | $\mu^+\mu^-$ | $e^\pm\mu^\mp$ | $e^+e^-$ | $\mu^+\mu^-$ | $e^\pm\mu^\mp$ |
| Two signal leptons | 402.1 | 521.6 | 741.3 | 313.7 | 392.6 | 553.8 |
| Jet veto | 198.6 | 258.6 | 370.1 | 122.0 | 142.5 | 205.7 |
| $Z$ veto | 165.0 | 212.0 | 370.1 | 99.0 | 115.8 | 205.7 |
| $p_{\mathrm{T},\ell\ell} > 80$ GeV | 28.0 | 35.3 | 57.0 | 15.9 | 17.2 | 30.2 |
| $E_{\mathrm{T}}^{\mathrm{miss,rel}} > 80$ GeV | 14.7 | 22.8 | 35.7 | 7.5 | 12.2 | 20.3 |
| $m_{\ell\ell} < 120$ GeV | 9.2 | 16.4 | 24.4 | 4.3 | 8.1 | 15.8 |

| Signal model | S2 | | |
|---|---|---|---|
| Lepton flavour | $e^+e^-$ | $\mu^+\mu^-$ | $e^\pm\mu^\mp$ |
| Two signal leptons | 139.6 | 168.7 | 253.8 |
| Jet veto | 65.7 | 78.2 | 118.6 |
| $Z$ veto | 55.5 | 65.5 | 118.6 |
| $m_{\mathrm{T2}} > 90$ GeV | 4.5 | 5.2 | 8.0 |
| $m_{\ell\ell} < 170$ GeV | 3.9 | 4.5 | 7.2 |

| Signal model | S3 | | |
|---|---|---|---|
| Lepton flavour | $e^+e^-$ | $\mu^+\mu^-$ | $e^\pm\mu^\mp$ |
| Two signal leptons | 40.9 | 46.3 | 71.1 |
| Jet veto | 17.5 | 20.7 | 30.8 |
| $Z$ veto | 15.5 | 18.0 | 30.8 |
| $m_{\mathrm{T2}} > 100$ GeV | 2.4 | 2.8 | 4.6 |

Expected numbers of signal events after each step of the event selection for benchmark model points in the SR-WW. The numbers are scaled to correspond to an integrated luminosity of 20.3 fb⁻¹. The signal models S1, S2 and S3 are chargino-pair production with wino chargino1 and bino neutralino1 with (m(chargino1),m(neutralino1))=(100,0) GeV, (140,20) GeV and (200,0) GeV, respectively. The GMSB model has m(chargino1) = 110 GeV, m(neutralino1) = 113 GeV , and the LSP is a massless gravitino.

Expected numbers of signal events after each step of the event selection for benchmark model points in the SR-Zjets. The numbers are scaled to correspond to an integrated luminosity of 20.3 fb⁻¹. The signal models S1 and S2 are neutralinos-chargino-pair production with wino chargino1 and bino neutralino1 with (m(chargino1),m(neutralino1)) = (250,0) GeV and (350,50) GeV, respectively.